UNIVERSITY OF CALIFORNIA,
IRVINE

Modeling of the Beam Emitted by Electrospray Thrusters

THESIS

submitted in partial satisfaction of the requirements
for the degree of

MASTER OF SCIENCE

in Mechanical and Aerospace Engineering

by

Marc Galobardes Esteban

Thesis Committee:
Manuel Gamero Castaño, Chair
Roger Rangel
Yun Wang

2023

TABLE OF CONTENTS

LIST OF FIGURES

ACKNOWLEDGMENTS

I would like to take this opportunity to express gratitude to, Professor Manuel Gamero Castaño. His unwavering support, invaluable guidance, and extensive knowledge have played a pivotal role in propelling this project forward. I am truly grateful for all that I have learned under his mentorship and for the continued growth and learning experiences that lie ahead.

In addition, I would like to extend my sincere thanks to my labmates, Albert Cisquella, Marco Magnani, Manel Caballero, and Kaartkey Misra. Their collaboration, and support have been fundamental in creating a vibrant and enriching research environment.

I cannot overstate the importance of the encouragement I have received from my family and friends. Their constant belief in me, their support during challenging times, and their celebration of my achievements have been invaluable.

Finally, I would like to express my deepest gratitude to the Balsells Foundation and the Melucci Fellowship for their generous financial support. Their assistance has alleviated the financial burden associated with my research endeavors, allowing me to focus wholeheartedly on the project. Their investment in my education and future is sincerely appreciated and will undoubtedly have a lasting impact on my academic and professional growth.

Once again, I would like to thank each and every individual and organization mentioned above for their indispensable contributions to my academic journey.

Some parts of the thesis have been reproduced from Gamero-Castaño, M., & Galobardes-Esteban, M. (2022). Electrospray propulsion: Modeling of the beams of droplets and ions of highly conducting propellants. Journal of Applied Physics, 131(1), 013307, with the permission of AIP Publishing.

ABSTRACT OF THE THESIS

Modeling of the Beam Emitted by Electrospray Thrusters

By

Marc Galobardes Esteban

Master of Science in Mechanical and Aerospace Engineering

University of California, Irvine, 2023

Manuel Gamero Castaño, Chair

Electrospray propulsion stands out as a unique electric propulsion technology, particularly well-suited for the growing popularity of SmallSats, spacecraft with a mass below 500 kg. Microfabrication techniques are used to create highly dense arrays of emitters allowing to scale up the thrust and process the low power available in SmallSats while maintaining a very high efficiency. However, in electrospray propulsion, overspraying of the extractor and accelerator electrodes poses a significant challenge, as the accumulation of fluid on these electrodes can lead to the formation of electrically conducting films and the catastrophic shorting of power supplies. Therefore, it is crucial to have a detailed understanding of the physics of the beam and the ability to model it accurately to design electrodes effectively and predict potential impingement during the long operational periods typical of electric thrusters, which can span several years. The model presented is used to study the composition of the beam emitted by the microfabricated electrospray thruster developed by our group. The model combines two different approaches: a Lagrangian model for the inner region near the jet breakup where the trajectories of all individual charged droplets are integrated simultaneously, and where Coulomb repulsion between droplets is fully captured while integrating the equations of motion; and an Eulerian model for the outer region where the structure of the beam is obtained by computing the envelopes of beamlets in which the population of droplets is subdivided. The two regions are coupled by the initial conditions

of the envelopes, which are calculated with the solution of the inner problem; and by the influence of the space charge of each region on the electric field. This strategy greatly reduces the computational time and allows to simulate the whole beam while retaining the important particle-on- particle Coulomb interaction where is significant.

Chapter 1

Introduction

1.1 Overview

The rise in space activity in recent years can be attributed to the affordability of commercial rocket launchers and the development of smaller satellites known as SmallSats. These SmallSats, categorized by weight as PicoSats ($<$ 1 kg), NanoSats ($<$ 10 kg), MicroSats ($<$ 200 kg), and MiniSats ($<$ 600 kg), have gained popularity due to their reduced costs and their innovative applications. In 2010, only 20 of these satellites were launched, but last year the number exceeded 1700 [16]. This surge in SmallSat usage has made it the go-to option for companies, countries, and global research groups looking to enter space exploration. The global SmallSat market was valued at $3.25 billion in 2020 and is expected to reach $13.71 billion by 2030, with a compound annual growth rate (CAGR) of 16.4% [1, 16, 51].

Constellations of tens/hundreds of SmallSats operating in precise orbits are likely to drive the market, and for these missions, on-board propulsion is an essential capability. Ninety-three operators are planning to launch constellations of 20 or more SmallSats, for a total estimate of 44,000 satellites from 2013 to 2040 [17].

However, despite their advantages, the lack of efficient propulsion systems poses a major obstacle to the effective utilization of SmallSats. On-board propulsion plays a vital role in SmallSat missions, enabling orbit rising, orbital maintenance, collision avoidance capabilities, and controlled deorbiting at the end of a satellite's mission. In fact, propulsion has become increasingly critical and necessary.

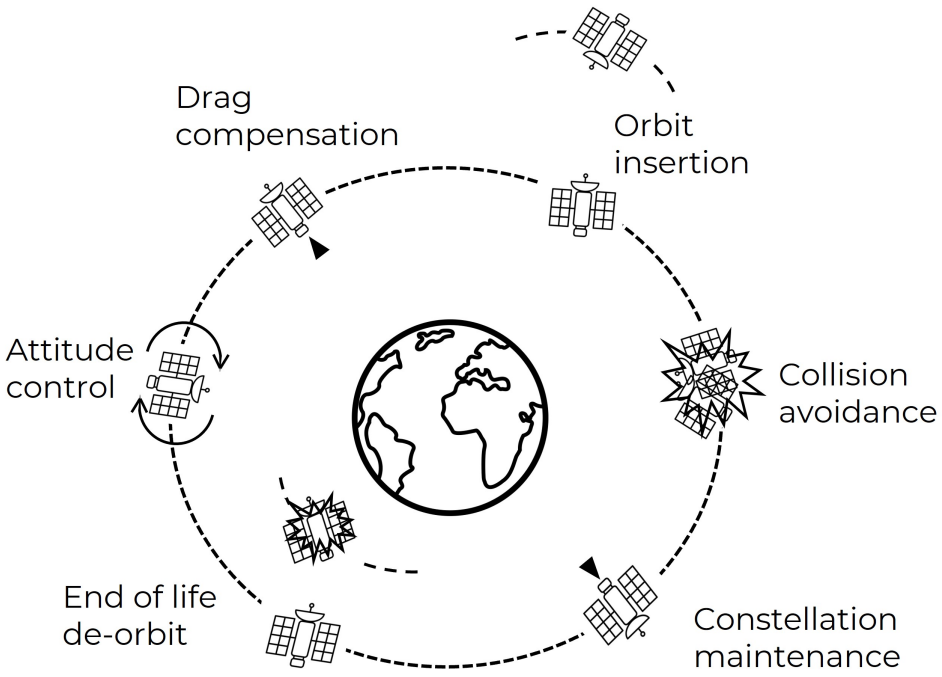

Figure 1.1: Illustration of the most relevant orbital maneuvers of interest for a spacecraft in LEO.

Small satellites are often secondary payloads, with the primary focus of launcher missions being the delivery of the primary payload to its intended orbit. Consequently, the orbit of interest for the primary payload may not align with that of the secondary payload. While launchers attempt to accommodate the needs of secondary payloads, it is not always possible. If a secondary payload is equipped with a propulsion system capable of performing orbit-rising maneuvers, it can independently transition from the insertion orbit to the final orbit. This capability is highly desirable for small satellites since without it, they are left

with limited options. Firstly, they can adapt their mission to the insertion orbit, although this may not be optimal. Secondly, they can opt for a costly private launch to be inserted directly into the desired orbit. This approach is both expensive and time-consuming, especially if a satellite operator aims to deploy a constellation rather than a single satellite. The third option involves employing a space tug, a larger spacecraft capable of transporting multiple small satellites to their final orbits. While this option is cheaper than dedicated launches, it still incurs costs and extends mission timelines due to the need for the space tug to visit multiple orbits for satellite deployment.

Furthermore, small satellite operators are interested in having orbital maintenance capabilities in their satellites. Low Earth Orbit (LEO) is the preferred orbit for many small satellite missions due to its accessibility, low energy requirements for placement, easy data transmission (high bandwidth, low communication latency), and improved image resolution for Earth observation applications. However, LEO orbits have two significant drawbacks: limited field of view, which means satellite constellations are needed for continuous coverage, and orbital decay caused by atmospheric drag. Counteracting this drag is crucial as it extends the mission lifetime, enabling satellites to operate for longer periods. In the past, missions were planned to be accomplished within the time that nature allowed, particularly when most of the missions had a scientific objective. As long as the required data could be obtained within the natural lifetime of the satellite in a specific orbit, there was limited interest in including a propulsion system to compensate for the drag due to the complications and expenses associated with it. However, with the growing commercial interest in LEO, increasing mission lifetimes has become a highly desirable feature. Prolonged operational periods translate to higher revenue and profitability, aligning with the ultimate goals of these satellites.

Finally, propulsion plays a crucial role in ensuring the sustainability of Low Earth Orbit (LEO), which is facing increasing congestion and hazards. Throughout the history of human

space exploration, a significant amount of space debris has accumulated and continues to orbit the Earth. This debris includes nonfunctional spacecraft, abandoned launch vehicle stages, satellite collisions, and fragments ranging from tiny paint flecks to unburned particles from solid rocket motors. Cleaning up this orbital debris is an extremely complex and expensive task. Currently, the main approach is to mitigate its effects and avoid making the problem worse. Propulsion is a key component in achieving these goals. Satellites equipped with propulsion systems have the ability to perform collision avoidance maneuvers, avoiding collisions with space debris or other operational satellites. Additionally, propulsion enables spacecraft to be safely and intentionally deorbited at the end of their missions, ensuring controlled disposal into the Earth's atmosphere. Due to the continuous increase in satellite launches, the issue of space debris has become a significant concern for organizations, leading them to revise regulations in order to mitigate its accumulation. For instance, the Federal Communications Commission (FCC) now requires all satellites to be deorbited within five years after the completion of their missions, reducing the previous limit of 25 years. These measures aim to address the pressing challenge of space debris and prevent further escalation of its quantity.

Traditionally, chemical propulsion has been the go-to choice for space propulsion in most satellites. However, chemical propulsion is not an optimal solution for SmallSats due to several reasons. Firstly, most orbit insertions require high delta-v, which cannot be efficiently achieved using chemical propulsion due to its low specific impulse (Isp). Implementing chemical propulsion would require allocating a significant portion of the SmallSat's mass for propellant. Secondly, rocket launchers often prohibit the inclusion of chemical propulsion systems in secondary payloads like SmallSats due to risks associated with the primary payload. Lastly, the high thrust associated with chemical propulsion is incompatible with precise drag compensation and precise attitude control maneuvers.

Electric propulsion (EP) presents a solution to these challenges by offering high Isp and low

thrust. The specific impulse indicates the efficiency with which propellant is utilized. EP requires less propellant for orbital maneuvers, but the trade-off is that these maneuvers take a longer time due to the low thrust associated with EP technologies. However, most EP technologies rely on plasma discharge chambers to ionize the propellant, and these chambers cannot be miniaturized to operate within the power range available to SmallSats, which can vary from 1-2 W in CubeSats to a few tenths of watts in Microsats. Electrospray propulsion, ESP, is unique among EP technologies because it does not require a plasma discharge, and therefore is amenable to miniaturization.

Electrospray thrusters are electrostatic accelerators of charged droplets and ions generated by electrosprays [24]. A single emitter operates at the micronewton and milliwatt levels, with a propulsive efficiency exceeding 70% and a tunable Isp ranging from 250 s to 2000 s. In order to process the power available in SmallSats and achieve higher thrust, a large number of emitters must be used to atomize the propellant [40, 41, 42, 7]. Because of its unique efficient performance at power levels as low as 1 mW, and the straightforward scalability of power and thrust made possible by microfabrication, ESP is the ideal propulsion technology for SmallSats. Furthermore, the low thrust associated with a single emitter (of the order of 1 μN) combined with its high stability enables precision spacecraft positioning applications. This technology has been demonstrated by the Disturbance Reduction System-Space Technology 7 mission (DRS-ST7), a precursor of the Laser Interferometer Space Antenna mission (LISA) [15, 62].

Electrosprays operating in cone-jet mode [8] atomize the liquid propellant into submicrometric droplets [14] with narrow distributions of diameters and charge-to-mass ratios. This is the emission mode commonly used in electrospray propulsion. In an experimental setting, the liquid is typically fed through a capillary tube at a higher potential than a nearby plate, and the electric field shapes the liquid into a conical meniscus as it flows out of the tip. A thin jet forms at the vertex of the so-called Taylor cone and, through a breakup caused by

capillary instability, generates charged droplets. Molecular ions are also emitted from the droplets and possibly from the surface of the jet as well [26]. The electric field accelerating the droplets and ions is induced by both the electric potentials set at the electrodes and the charges carried by the particles in the beam. The contribution of this space charge is key to the radial expansion of the beam [9]. Particle-on-particle Coulombic repulsion dominates the initial region of the beam following the emission point [18]. This initial region is small compared to other characteristic lengths of the electrodes such as the gaps between the emitter, extractor and accelerator electrodes, and the diameters of the emitter and the orifices of the extractor and accelerator. Figure 1.2 shows an image of an electrospray operating under vacuum conditions [24]. From left to right: the capillary emitter (approximately 1mm outer diameter), the Taylor cone, and the beam of droplets and ions.

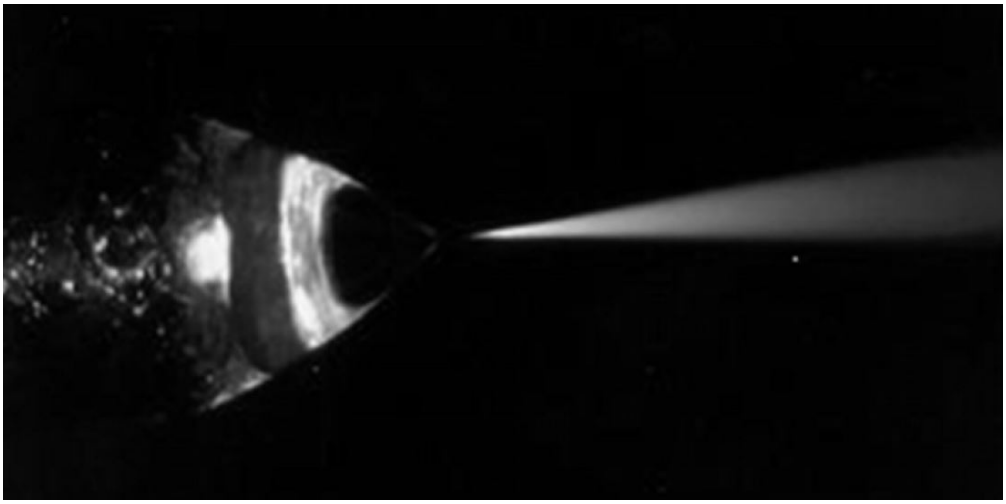

Figure 1.2: Electrospray in vacuum. From left to right: capillary emitter (approximately 1mm outer diameter), Taylor cone, and beam of droplets and ions.

1.2 Background

Electrospray atomization has been presented as a well-suited method for spacecraft propulsion but the ability to produce ions and charged droplets of controllable diameters down to

a few nanometers also has important technological applications in nanoparticle generation and deposition [52, 37, 49, 5, 36], mass spectrometry [13, 12, 50, 3], sputtering [25, 55], electrospinning of nanofibers [6, 11] and biomedical and drug delivery applications [39, 56, 60]. All applications are dependent on how the droplets distribute themselves within the spray plume. Therefore, predicting the structure of the electrospray plume has been a topic of interest for the last two decades.

Experimental techniques for studying electrospray plumes are mostly based on optical imaging, pulsed shadowgraphy [32, 38, 47], high-speed video [34] and phase Doppler anemometry [56, 27, 33, 46]. In pulsed shadowgraphy, a short-duration, high-intensity light pulse (typically from a flash lamp or laser) is directed through the medium of interest. The density variations within the medium cause changes in the refractive index, leading to the bending and scattering of light rays. Shadowgraph images reveal more details than optical images. This technique has been used for example to rapidly evaluate the effects of different modes of electrospray operation [47]. Phase Doppler Anemometry (PDA) is a laser-based measurement technique used to analyze the properties of particles in a fluid flow. It provides information about particle size, velocity, and concentration by utilizing the principles of interferometry and light scattering. In PDA, a laser beam is split into two beams: a reference beam and a measurement beam. The measurement beam is directed towards the region where particles are present. When the particles intersect the measurement beam, they scatter light. The scattered light from the particles interferes with the reference beam, forming a pattern of constructive and destructive interference known as an interferogram. By analyzing the interferogram, PDA can determine the phase difference between the scattered light and the reference beam. This phase difference is related to the particle properties, such as size and velocity. PDA is capable of sensing at high rates (e.g. 104 droplets s^{-1}), and covers a wide range of droplet diameters, from 0.2 to 300 μm [46]. However, this technique cannot measure the region immediately after the jet breakup due to the high droplet density,

instead, they measure at a few mm downstream of the jet breakup.

Numerical models complemented with experimental measurements are able to provide information at the emission point. The sprays of charged droplets produced by electrosprays have been numerically modeled mostly under atmospheric conditions [54], since most of the applications mentioned before do not require to operate under vacuum. However, models that have been proposed to study electrosprays in vacuum can easily adapt the governing equations to include the effects of a surrounding atmosphere. The drag coefficient is taken usually for an isolated solid sphere moving through uniform gas flow and is a function of the Reynolds number [31]. The numerical approaches can be classified into two groups: the Eulerian models, which predict the droplet number density as a continuous function of space and time, by integration of mass and momentum conservation equations, plus Gauss' law for the electric potential (Poisson's equation)[35, 18]; and the Lagrangian models, in which the individual trajectories of all the droplets in the spray are solved in 3D space using Newton's equation of motion. The electrospray plume was first modeled by Gañán-Calvo et al. [27] using a Lagrangian approach, but the set of ordinary differential equations could not be solved for a large enough number of droplets to represent the space charge effect. By the end of the 2000s, simplified Lagrangian models and more computational power enabled the simulation of electrosprays emitting thousands of droplets [10, 48], and the models were used to predict deposition patterns [61]. The computational time scales with the square of the number of droplets due to their mutual interaction. Therefore, simulating electrosprays of submicrometric droplets is challenging due to the very large number of droplets present in typical regions of interest. This problem can be alleviated by using different integration time-steps throughout the computational domain [31]. Lagrangian models could predict size segregation for main droplets and the contribution of space charge to the electric field, which has been observed to have a key role in the expansion of droplets and ions in the radial direction [18, 56]. An Eulerian model [35] can provide insights and realistic results at a fraction of the cost of a Lagrangian simulation, but cannot fully capture the coupling between moving

droplets.

1.3 Motivation

Overspraying of the extractor and accelerator electrodes is a major lifetime-limiting mechanism in electrospray propulsion [63]. The progressive accumulation of fluid on these electrodes leads to the formation of electrically conducting films and the catastrophic shorting of power supplies; it may also lead to backspraying between the grids and the emitter electrode, and erratic and progressive worsening of the performance of the thruster [57]. Having a detailed first-principles understanding of the physics of the beam and the capability to model it is important to properly design the electrodes and to predict potential impingement of the beam during the long periods of operation, often several years, typical of electric thrusters [30].

The model presented combines two different approaches: a Lagrangian model for the inner region near the jet breakup where the trajectories of all individual charged droplets are integrated simultaneously, and where Coulomb repulsion between droplets is fully captured while integrating the equations of motion; and an Eulerian model for the outer region where the structure of the beam is obtained by computing the envelopes of beamlets in which the population of droplets is subdivided. The two regions are coupled by the initial conditions of the envelopes, which are calculated with the solution of the inner problem; and by the influence of the space charge of each region on the electric field. This strategy greatly reduces the computational time while retaining the important particle-on-particle Coulomb interaction where is significant. Finally, the numerical solution is validated with experimental results obtained with the ionic liquid 1-ethyl-3-methylimidazolium bis(trifluoromethylsulfonyl)imide, EMI-Im [44], which is the propellant used by the electrospray thruster recently demonstrated by the

DRS-ST7 mission and whose beams have been characterized in detail [19, 21, 22, 58, 45]. EMI-Im produces a particular type of beam consisting of a mixture of charged droplets and molecular ions without significant spatial separation. There exist other prototypical cases such as ion beams devoid of charged droplets [43], beams of main and satellite droplets that are spatially separated [18], electrosprays at atmospheric pressure [28], etc. that can be studied with the present model by using the appropriate initial conditions and distributions for the constituent particles.

This thesis presents the outcomes achieved by applying the model to the microfabricated electrospray source geometry developed within our research group [7]. The primary objectives are to predict beam interception at the extracting electrodes and investigate beam expansion when the source operates in various configurations. Chapter 2 provides an overview of the governing equations employed in the model, the numerical scheme employed for problem solving, and the essential experimental input parameters necessary for conducting the simulations. In Chapter 3, a comprehensive analysis of the beam composition is presented, highlighting the underlying mechanisms involved. Additionally, different operation modes and electrode configurations are explored.

Chapter 2

Beam Model

2.1 Beam regions and model equations

The position $\mathbf{x}_i$ of the i^{th} droplet can be computed by integrating its equation of motion

$$\frac{d^2\mathbf{x}_i}{dt^2} = \xi_i \mathbf{E}(\mathbf{x}_i), \tag{2.1}$$

where the electric field $\mathbf{E}$ is induced by the distribution of charges on the surfaces of the electrodes, on the cone-jet and throughout the beam.

The solution for the Poisson equation for the electric potential ϕ

$$\nabla^2\phi(\mathbf{x}) = -\sum_{\text{all } i} \frac{q_i \delta\left(\mathbf{x} - \mathbf{x}_i\right)}{\varepsilon_0} \tag{2.2}$$

yields the electric field $\mathbf{E}$

$$\mathbf{E} = -\nabla\phi \tag{2.3}$$

where q is the charge of a droplet, δ the Dirac-delta function, and ε_0 the vacuum permittivity.

Integrating Eq. 2.1 throughout the whole domain would be the most accurate way to solve the problem. However, it is not possible to do it because of the large computational cost that it would have. Integrating Eq. 2.1 scales as N^2, being N the number of droplets in the domain. It requires solving the Poisson equation for each droplet in the domain at every time step. Moreover, it will be shown in this report that it is not necessary to take into account the contribution of all droplets in the domain to obtain an accurate result. Only droplets that are close to each other produce a significant effect that needs to be captured.

Our model divides the computational domain into two regions to overcome this problem: an inner region near the jet breakup where the trajectories of all individual charged droplets are integrated simultaneously and where Coulomb repulsion between droplets is fully captured and an outer region where the structure of the beam is obtained by computing the envelopes of beamlets in which the population of droplets is subdivided. The inner region is a Lagrangian model, i.e. time-dependent, and very small and the outer region is an Eulerian model, i.e. time-independent, and occupies most of the domain. The initial conditions required for the Lagrangian model are found experimentally whereas the initial conditions of the Eulerian model are the output of the first.

Eq. 2.1 is solved in a dimensionless form in the model. The electric field is a decomposed into two terms: a term for the electric field induced by the surrounding droplets, i.e. the space charge, $\mathbf{E}_{SC}$; and a term for the electric field induced by the electrodes, $\mathbf{E}_{ext}$.

The equation of motion in vectorial form for one droplet is described in Eq. (2.4).

$$m_i \frac{d^2\mathbf{x}i}{dt^2} = q_i \ \mathbf{E}_{SC} + q_i \ \mathbf{E}ext = qi \sum_{j=1}^{N(j\neq i)} \frac{q_j}{\epsilon_0 4\pi} \frac{\mathbf{x}_i - \mathbf{x}_j}{|\mathbf{x}_i - \mathbf{x}j|^3} + q_i \ \mathbf{E}_{ext} \tag{2.4}$$

where:

m_i is the mass of the droplet.

$\mathbf{x_i}$ is the position vector of the droplet in Cartesian coordinates.

$\mathbf{x_j}$ is the position vector of the surrounding droplets in Cartesian coordinates.

q_i is the electric charge of the droplet.

q_j is the electric charge of the surrounding droplets.

ϵ_0 is the vacuum permittivity.

N is the number of droplets in the domain.

The following characteristic parameters are used to write the equation of motion in a dimensionless form.

- **Characteristic length:** $L_c = \lambda_c$

  Each droplet has an associated wavelength and λ_c is the wavelength associated with the most likely droplet to be produced. The droplet's wavelength is directly related to the diameter of the droplet. The mass of the droplet must correspond to the mass of a fraction of the jet. Figure 2.1 shows an illustration to clarify the concept

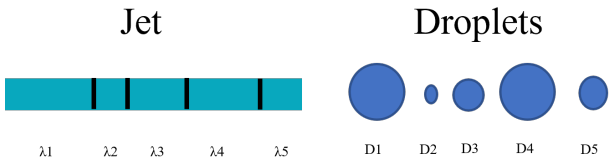

Figure 2.1: Illustration of wavelengths associated to droplets.

  λ_c is obtained from the diameter of the most likely droplet produced by the breakup of the jet D_{crit}, Eq. 2.5. The detailed explanation of how D_{crit} is obtained is presented in Section 2.2.

$$\lambda_c = \frac{2}{3}\frac{D_{crit}^3}{D_J^2} \tag{2.5}$$

- **Characteristic velocity:** $V_c = v_J$

  v_J is the velocity of the jet at the breakup point and it is estimated through experimental measurements. Section 2.2 provides a detailed explanation of how v_J is obtained.

- **Characteristic time:** t_c

  The characteristic time is defined as:

$$t_c = \frac{L_c}{V_c} = \frac{\lambda_c}{v_J} \tag{2.6}$$

  The characteristic time gives us an approximation of how long it takes for the droplet to be emitted.

- **Characteristic charge to mass ratio:** $\xi_c = \xi_j$

  By doing the derivative of ξ with respect to time, we can express ξ as a function of current I and mass flow rate $\dot{m}$, which leads to obtaining ξ_j from the current of the beam I_b, the volumetric flow rate of the ionic liquid Q and its density ρ.

$$\xi_j = \frac{q}{m} = \frac{I}{\dot{m}} = \frac{I_b}{\rho\, Q} \tag{2.7}$$

- **Characteristic charge:** $q_c = q_j$

  q_j is the charge of an average droplet, it is defined by the mass of the most likely droplet to be produced and the charge-to-mass ratio of the jet ξ_J

$$q_j = \frac{\pi}{6} D_{crit}^3\, \rho\, \xi_J \tag{2.8}$$

- **Characterisitc Electric field:** E_c

The characteristic electric field is defined as the ratio between the potential of the emitter V_e and the radius of the Taylor's cone meniscus r_m, which is essentially the radius of the tip of the emitter.

$$E_c = \frac{V_e}{r_m} \tag{2.9}$$

Once the dimensionless parameters are introduced in Eq. (2.4), dimensionless coefficients appear: π_C and π_X.

Eq. (2.10) is the equation of motion in dimensionless form.

$$m_i \frac{d^2\mathbf{x_i}}{dt^2} = \pi_C \; \xi_i \sum_{j=1}^{N(j\neq i)} q_j \frac{\mathbf{x_i} - \mathbf{x_j}}{|\mathbf{x_i} - \mathbf{x_j}|^3} + \pi_{XT} \; \xi_i \; \mathbf{E}_{ext} \tag{2.10}$$

where:

$$\pi_C = \frac{\xi_c \; t_c^2 \; q_c}{4\pi\epsilon_0 \; L_c^3} \tag{2.11}$$

$$\pi_{XT} = \frac{E_c \; \xi_c \; t_c^2}{L_c} \tag{2.12}$$

Applying the above-mentioned definitions of the characterisitic parameters to Eq. (2.11) and to Eq. (2.12), it yields Eq. (2.13) and Eq. (2.14), respectively.

$$\pi_C = \frac{1}{\rho \; 4\pi\epsilon_0} \frac{I_b^2}{Q \; v_j^3} \tag{2.13}$$

$$\pi_{XT} = 12\pi^2 \frac{\epsilon_0 \gamma}{\rho} \frac{V_e}{r_m} \frac{D_J^2}{I_b Q} \tag{2.14}$$

The parameter π_C provides insights into the relationship between potential energy and kinetic energy within a system. Specifically, it indicates the relative strength of the electric interaction compared to the droplet's kinetic energy. It enables a comparison between the contributions of the space charge and the electrodes to the electric field at the emission point, in conjunction with π_{XT}. Notice the strong dependence of π_C on the velocity of the jet v_J, which is a parameter that is not straightforward to obtain experimentally.

The following sections will explain how the model is solved in the inner region and in the outer region.

2.1.1 Grid

The model uses a spherical grid to discretize the domain, it only needs to extend to the region occupied by the beam. The grid, shown in Figure 2.2, is used to discretize the space charge and to evaluate the electric field at the nodes. Discretizing the space charge allows us to compute the electric field induced by the droplets in a more efficient way. The electric field induced by the droplets surrounding the point of interest is calculated in an exact manner using two-body Coulomb potentials and the contribution of the rest of the droplets is distributed as an axisymmetric load, producing an axisymmetric electric field.

Figure 2.3 shows the boundary between the inner region and the outer region. The effect of the space charge is most important in the region near the emission point, hence, the grid is discretized in smaller cells. In the outer region, the effect of the space charge is less important and the cells of the grid can get progressively bigger in the axial direction without compromising the accuracy of the computed electric field. The usage of this grid with variable dimensions reduces the computational cost of the simulation.

The grid also allows computing the electric field at its nodes instead of computing it at the

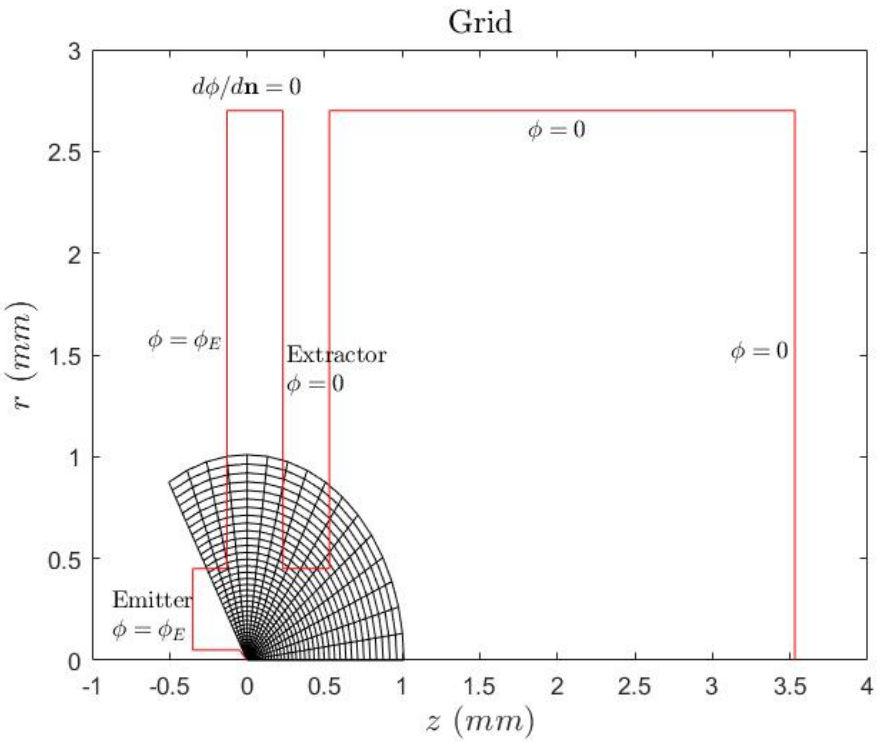

Figure 2.2: Computational domain and grid for discretizing the space charge and evaluating the electric field

exact position of the droplet. Then, the electric field at the exact position of each node is found by doing a bilinear interpolation. The most demanding computations of the electric field depend on the position where the electric field is being calculated. Therefore, if the electric field is calculated at the nodes of the grid, which are fixed for the entire simulation, the integrals found in these computations only need to be computed once, instead that at every time step.

2.1.2 Inner region

The equation of motion and the Poisson equation, Eq. 2.1 and Eq. 2.2, are solved in the inner region for a large sequence of droplets to retain individual particle-on-particle Coulomb interactions. The inner region is characterized by a high droplet population and is orders of magnitude smaller than the outer region, its characteristic length is 10 μm. This

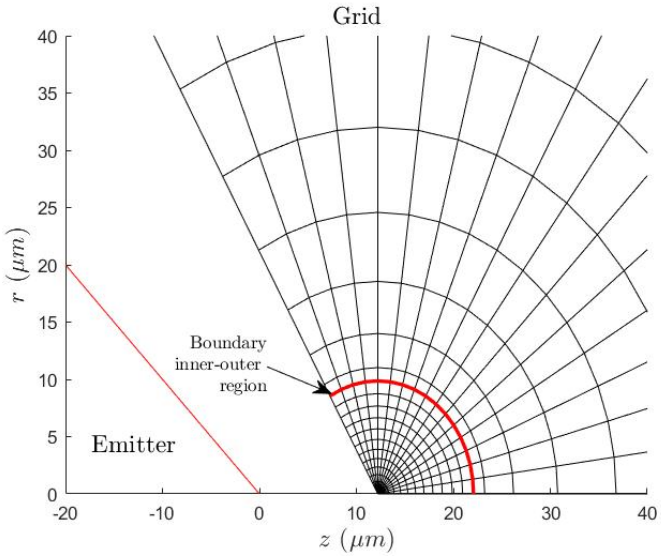

Figure 2.3: Close up of the emission area. Boundary between the the inner region and the outer region.

characteristic length can be evaluated with the solution, by finding the distance from the emission point where the radial component of the electric field induced by droplet-on-droplet Coulomb repulsion is a small fraction of the total value. See Section 3.1.

Although the breakup of the jet is time-dependent, we consider constant nominal values for its position z_J and for the velocity of fluid v_J. Moreover, for the highly conducting liquids of interest to electrospray propulsion, the jet has a substantial amount of charge on its surface, making it susceptible to lateral oscillations [22]. Its effect on the initial conditions of the droplets is implemented by assigning values that randomly deviate from the nominal breakup position and jet velocity:

$$\mathbf{x}_i(t_{o,i}) = z_J \mathbf{i}_z + \boldsymbol{\alpha}_i \tag{2.15}$$

$$\dot{\mathbf{x}}_i(t_{o,i}) = v_J \mathbf{i}_z + \boldsymbol{\beta}_i, \tag{2.16}$$

where $\boldsymbol{\alpha}_i$ and $\boldsymbol{\beta}_i$ are small offsets, and $\mathbf{i}_z$ the unit vector along the axial direction.

To determine the position of the breakup of the jet, the Laplace equation is solved to obtain the electric potential along the axis. The experimental measurement of the potential of the jet is then used to identify the corresponding axial position. The red dot in Figure 2.4 shows the axial position where the electric potential coincides with the potential of the jet ϕ_J.

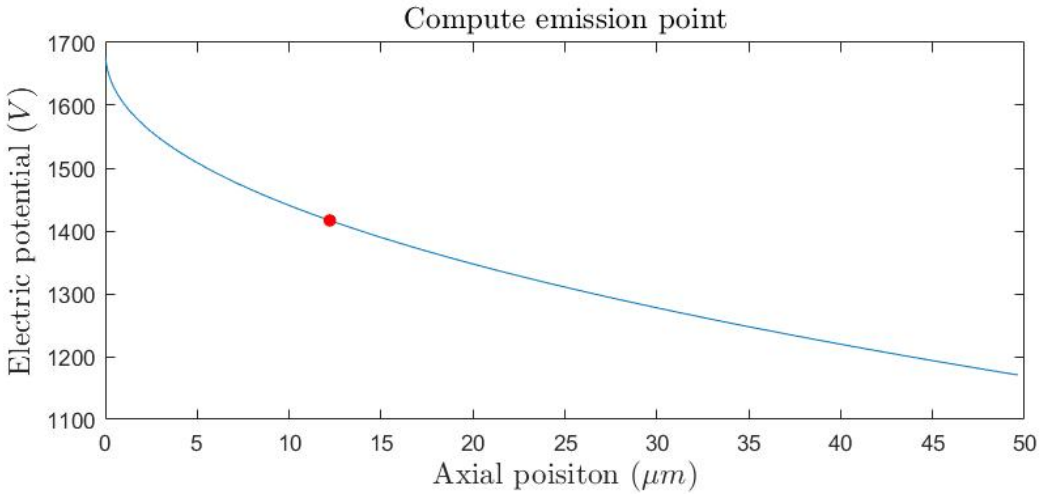

Figure 2.4: Electric potential along the axis and emission point marked with a red dot

The potential of the jet at the break-up point and the velocity of the jet are measured experimentally [22]. Section 2.2 briefly explains how these values are obtained.

The simultaneous integration of the trajectories of droplets in the inner region is done with the Störmer–Verlet method. The Störmer–Verlet method, also referred to as the velocity Verlet method, is a numerical integration algorithm that is commonly used to solve equations of motion in classical mechanics, such as Newton's equations, which describe the motion of particles under the influence of forces.

The basic idea behind the Störmer–Verlet method is to update the positions and velocities of the particles in a stepwise manner. Given the current positions and velocities of the particles at time t, the algorithm computes the new positions at time $t + \Delta t$, and then updates the velocities at time $t + \Delta t/2$ using the new positions. Finally, it updates the positions again at time $t + \Delta t$ using the updated velocities. Figure 2.5 shows a schematic diagram of how

the method works.

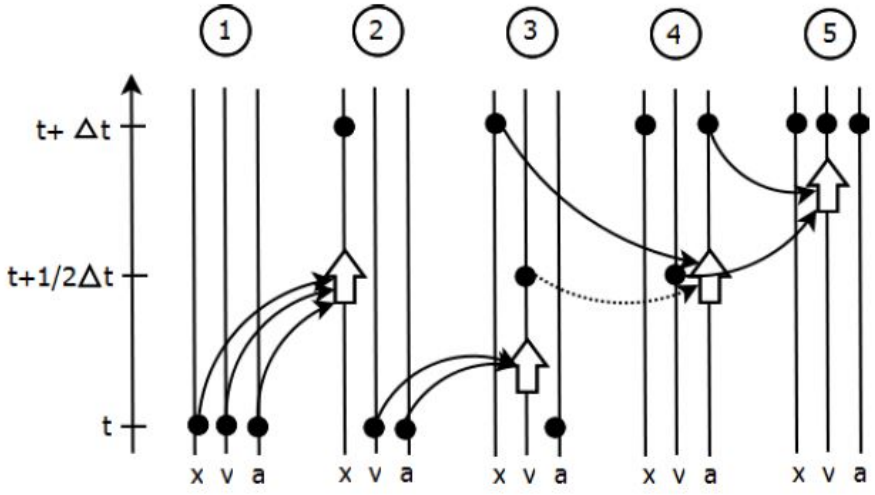

Figure 2.5: Schematic of the Störmer–Verlet method

1. Start from the initial system's setup

2. Calculate the new position

$$x(t + \Delta t) = x(t) + v(t)\Delta t + \frac{1}{2}a(t)\Delta t^2$$

3. Calculate the intermediate velocity

$$v\left(t + \frac{1}{2}\Delta t\right) = v(t) + \frac{1}{2}a(t)\Delta t$$

4. Calculate the new acceleration $a(t + \Delta t)$ since now the new position of particles is known.

5. Calculate new velocity

$$v(t + \Delta t) = v\left(t + \frac{1}{2}\Delta t\right) + \frac{1}{2}a(t + \Delta t)\Delta t$$

It is very important to choose an adequate time step for the numerical integration. If the time step is too large, the interaction between particles will not be captured, but if the time step is too small the computational cost will be unnecessarily high.

We employ a time step Δt based on the emission period of the critical droplet, typically $\Delta t = 0.01 t_c$, which is sufficient to produce a maximum error in the exit angle of the droplets' trajectories smaller than 1%. Using the characteristic time as a reference allows us to ensure that we are using a time step that has a physical meaning and that will be small enough to retain Coulomb interactions.

Computing the acceleration of the particles during the numerical integration of the equation of motion is obviously the most complicated and time-consuming part because it requires computing the electric field, which means solving the Poisson equation. Section 2.1.1 explains that in order to make the computation more efficient, the electric field is computed at the nodes of the grid, instead of computing it at the exact position of each droplet. It is easy to see with the most simple example, the fundamental solution of the Poisson equation, why applying this technique helps to reduce computational time.

The fundamental solution for the Poisson equation is obtained using Green's function

$$\phi = \frac{Q}{4\pi\epsilon_0 r} \tag{2.17}$$

ϕ is the electric potential induced at distance r from a central point charge Q. Since the Poisson equation is linear, we can apply the principle of superposition and obtain an expression for the electrical potential generated by discrete charges

$$\phi = \frac{1}{4\pi\epsilon_0} \sum_i \frac{q_i}{|\mathbf{r} - \mathbf{r}_i|} \tag{2.18}$$

and if instead of looking at discrete charges we consider a continuous charge distribution (q_i

becomes ρdV, where ρ is the volumetric charge density) we get

$$\phi = \frac{1}{4\pi\epsilon_0} \int_V \frac{\rho}{|\mathbf{r} - \mathbf{r}'|} dV \tag{2.19}$$

If we assume that the volumetric charge density does not depend on the position and is constant over the region that will be integrated, it yields an integral that only depends on geometric values. Therefore, the computation of the electric field only requires solving the integral one time, because the position of the evaluation point will not change.

$$\mathbf{E} = \frac{-\rho}{4\pi\epsilon_0} \int_V \nabla\phi dV \tag{2.20}$$

In our case, the volumetric charge density is computed from the charges that are in a particular cell, and at each time step it is only needed to update the net charge of each cell.

That was a very simplified explanation to help visualize why computing the electric field at the nodes of the grid, which are fixed, is very important to boost the computational speed of the code. However, in the model we must take into account the boundaries of the electrodes. The boundaries fix a potential across the domain, making the computation of the solution more complicated. It is not possible to solve it with an analytical function, therefore, we use the boundary element method with linear elements to solve the Poisson equation and evaluate the electric field. Brebbia and Dominguez [4] provide an excellent description of the technique, and Bakr [2] focuses on its application to axisymmetric geometries such as the one considered here. For a given charge density field, the potential and the electric field at any point inside the simulation domain are computed with boundary integrals involving the potential and its gradient normal to the boundary, and the position of the point.

The evaluation of the integral requires the discretization of the boundary into N_Γ nodes: of the $2 \times N_\Gamma$ values of the potential and the normal gradient needed to compute the integral,

N_Γ values are specified as boundary conditions, while the remaining N_Γ values must be computed by considering each node as the load point in the boundary integral. This results in a system of N_Γ linear algebraic equations for the unknown potentials and gradients. Using $\mathbf{u}$ to denote the vector of unknowns (a subset of the potentials and gradients at the nodes), $\mathbf{w}$ for the vector of specified boundary conditions, and $\mathbf{q}$ for a vector with the net charge inside the cells of the grid (see Fig. 2.2), the system of algebraic equations and its solution can be written as

$$\mathbf{A} \cdot \mathbf{u} = \mathbf{B} \cdot \mathbf{w} + \mathbf{M} \cdot \mathbf{q} \quad \longrightarrow \quad \mathbf{u} = \mathbf{A}^{-1} \cdot (\mathbf{B} \cdot \mathbf{w} + \mathbf{M} \cdot \mathbf{q}). \tag{2.21}$$

After separating $\mathbf{u}$ and $\mathbf{w}$ into vectors $\boldsymbol{\phi}_\Gamma$ and $\mathbf{e}_\Gamma$ with the potentials and gradients at the boundary nodes, the potential field at any point $\mathbf{x}$ is computed explicitly as:

$$\phi_{2D}(\mathbf{x}) = \mathbf{g}(\mathbf{x}) \cdot \boldsymbol{\phi}_\Gamma + \mathbf{h}(\mathbf{x}) \cdot \mathbf{e}_\Gamma + \mathbf{m}(\mathbf{x}) \cdot \mathbf{q}, \tag{2.22}$$

with similar equations for the components of the electric field. Note that the potential is two dimensional (axisymmetric). The elements of the matrices $\mathbf{A}$, $\mathbf{B}$ and $\mathbf{M}$, and the vectors $\mathbf{g}$, $\mathbf{h}$ and $\mathbf{m}$ are geometric factors that only depend on the discretization of the boundaries, the mesh used to discretize the space charge and, in the case of $\mathbf{g}$, $\mathbf{h}$ and $\mathbf{m}$, on the evaluation point. Therefore these matrices and vectors only need to be computed once in the initial step of the calculations.

Equations (2.21) and (2.22) assume a continuous space charge field which, combined with the axisymmetric geometry, result in a smooth and axisymmetric electric field. This is appropriate for the outer region of the beam model. However, droplet-on-droplet Coulomb interactions are retained in the inner region, resulting in a three dimensional electric field. To account for this we define a spherical neighborhood around each droplet with a cut-off radius r_{cf}, and compute the contribution to the field by neighboring droplets as a direct sum

of pair potentials

$$\phi_{3D}(\mathbf{x}_i) = \phi_{2D}(\mathbf{x}_i) + \sum_{j}^{\|\mathbf{x}_i - \mathbf{x}_j\| < r_{cf}} \frac{q_j}{4\pi\varepsilon_0 \|\mathbf{x}_i - \mathbf{x}_j\|}. \tag{2.23}$$

When computing the Coulomb field induced by neighboring droplets we subtract their contribution to the axisymmetric field, in order to avoid double-counting. In summary, we use the smooth electric field (2.22) when integrating the characteristics of the momentum equation in the outer region, and the three dimensional field (2.23) when integrating the trajectories of individual droplets in the inner region.

2.1.3 Outer region

In the outer region, the lower droplet density and the reduced importance of Coulomb scattering are compatible with a continuous model for the droplet velocity and charge density.

To solve the continuum, outer problem we separate the droplets into groups with constant charge-to-mass ratio ξ_k, and compute the volumetric charge density ρ_k and velocity $\mathbf{V}_k$ fields for each group. These fields fulfill conservation of charge and momentum:

$$\nabla \cdot (\rho_k \mathbf{V}_k) = 0 \tag{2.24}$$

$$\mathbf{V}_k \cdot \nabla \mathbf{V}_k = \xi_k \mathbf{E}, \tag{2.25}$$

where the Poisson equation for the electric potential

$$\nabla^2 \phi = -\frac{1}{\varepsilon_0} \left(\rho^{in} + \sum_{\text{all } k} \rho_k \right) \tag{2.26}$$

yields the electric field. The space charge term includes contributions from all droplet groups in the outer region, $\sum \rho_k$, as well as the space charge in the inner region, ρ^{in}. We use the

method of characteristics to integrate (2.25) for a given electric field, where the trajectory of any droplet with charge to mass ratio ξ_k is a characteristic curve of this partial differential equation. Once a set of characteristics is computed, the axial V_z and radial V_r components of the velocity field are obtained by integrating the ordinary differential equations

$$V_{z,k}\frac{dV_{z,k}}{dz} = \xi_k E_z \tag{2.27}$$

$$V_{r,k}\frac{dV_{r,k}}{dr} = \xi_k E_r \tag{2.28}$$

along the characteristics. The characteristics themselves are determined by integrating (2.1), starting at the boundary between the inner and outer regions. The required initial velocities are obtained by averaging the inner solution, which also yields the charge flux along the boundary. For example, the initial velocity $\mathbf{V}_{o,k}$ of a characteristic with a charge-to-mass ratio ξ_k at a particular position of the boundary is computed as the charge-weighed average of the velocities of all N individual droplets with that charge-to-mass ratio exiting within a small neighborhood of that position:

$$\mathbf{V}_{o,k} = \frac{\sum_i^N q_i \dot{\mathbf{x}}_i}{\sum_i^N q_i} \tag{2.29}$$

With this information we compute the two characteristics enveloping each droplet group, as well as additional characteristics in between. Once the velocity field $\mathbf{V}_k$ is determined along the characteristics, equation (2.24) readily yields the charge density field.

The characteristics are integrated in cylindrical coordinates using a fourth-order Runge-Kutta scheme with variable timestep.

2.2 Sequence of droplets and initial conditions

The model needs several experimental parameters to run the simulation; it requires values of the beam current I_b, the flow rate Q, the jet velocity V_J, the potential of the jet in the breakup region ϕ_J and the charge-to-mass ratio distribution ξ . These values are tabulated and explained in detail in Ref [22]. Since characterizing all possible beam currents is not feasible, the model utilizes interpolation techniques to determine the most accurate value. In order to make it easier for the reader, these parameters will first be presented and explained:

- **Current of the beam I_b**

  The current of the beam is one of the main parameters measured during the characterization of an electrospray source. As it will be shown in this report, it has an important effect on the divergence of the beam as well as on the determination of many other parameters of relevance.

- **Volumetric flow rate Q**

  The volumetric flow rate is related to the beam current emitted and it is determined through Eq. 2.30 from the applied pressure P and the hydraulic resistance of the line R_H, which was calibrated with a bubble flow meter [22].

$$Q = \frac{P}{R_H} \tag{2.30}$$

- **Velocity of the jet v_J, potential of the jet at the break-up point ϕ_J and charge-to-mass distribution ξ**

  The velocity of the jet v_J and the potential of the jet at the break-up point ϕ_J are not simple values to measure because it requires measuring the retarding potential in tandem with time-of-flight. The detailed description of the method to obtain these values and an analysis of the results can be found in Ref [22], here only a general description

will be provided.

Reference [22] tabulates v_J and the voltage drop along the cone-jet, $\phi_E - \phi_J$, for cone-jets of EMI-Im operated at 21 ^{o}C. ϕ_E and ϕ_J are the potential of the emitter and the potential of the jet at the breakup respectively. The experimental values range between 547 and 431 m/s, and 196 and 455 V, for beam currents between 230 and 450 nA. The values for a cone-jet with a current of 300 nA are $\mathrm{v}_J = 501$ m/s, $\phi_E - \phi_J = 274$ V.

The potential at which the droplets are accelerated is not the potential of the emitter because of the viscous and Ohmic losses occurring at the cone jet [20, 22], instead the droplets are being accelerated at ϕ_J. Figure 2.6 illustrates the process. The energy of what would be a droplet at point A is the product of its charge q and the potential of the emitter V_E. Heat losses across the Taylor cone yield lower energy at point B, which is the energy available to accelerate the droplet. At point C, the jet breaks up and the droplet starts flying, its energy is associated with its initial velocity v_J, and the electrostatic energy at the breakup point, which is the potential of the jet ϕ_J.

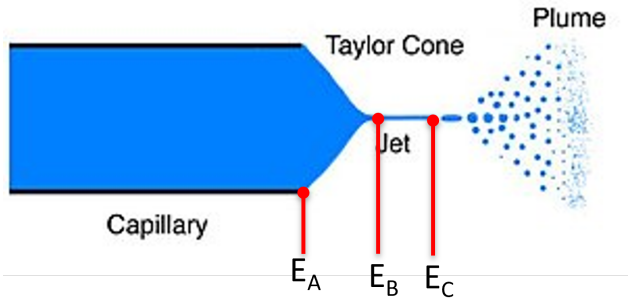

Figure 2.6: Energy losses occurring at the cone jet

The retarding potential of a charged particle, defined as the sum of its kinetic and potential energy divided by the charge

$$\phi_{\mathrm{RP}} = \frac{1}{2}\zeta v^2(\mathbf{x}) + \phi(\mathbf{x}) \tag{2.31}$$

is a constant of motion in an electrostatic field.

The technique of operating a RPA analyzer and TOF in tandem is based on the natural dispersion of the droplets' mass to- charge ratio induced by the breakup, and assumes that the variations of potential and droplets' velocities in the unsteady breakup region are much smaller than the voltage drop along the cone jet and the velocity gained by the liquid along the jet. Under these conditions all droplets produced by the breakup are emitted at approximately the same nominal potential ϕ_J and velocity v_J. Thus, if the retarding potentials and mass-to-charge ratios of many droplets emitted from the breakup region are available, ϕ_J and v_J can be obtained from the linear regression

$$\phi_{\mathrm{RP},i} = \frac{1}{2} v_J^2 \zeta_i + \phi_J \tag{2.32}$$

Figure 2.7 shows a schematic of the experimental setup. The plume emitted by the electrospray is intercepted by the electrostatic mirror with the purpose of only allowing droplets with a specific value of retarding potential to go through. The electrostatic mirror will deflect the trajectory of the droplets going in, and only those whose retarding potential coincides with the potential difference applied in the electrostatic mirror will go through the exit orifice. Then the time of flight of the droplets that go through will be measured with the help of an electrostatic gate. The electrostatic gate works by deflecting the beam that goes through the extracting orifice of the electrostatic mirror. If the gate is in the closed state, it will create an electric field that will deflect the beam preventing it from arriving at the collector, but if the gate is in the open state, no electric field will be created and the beam will continue on a straight line and will arrive at the collector. Therefore, it is possible to measure the time of flight distribution of the droplets that go through the gate.

RPA analysis in tandem with TOF yields a very accurate measurement of the charge-to-mass ratio distribution of the plume emitted by the electrospray, which is needed to obtain the

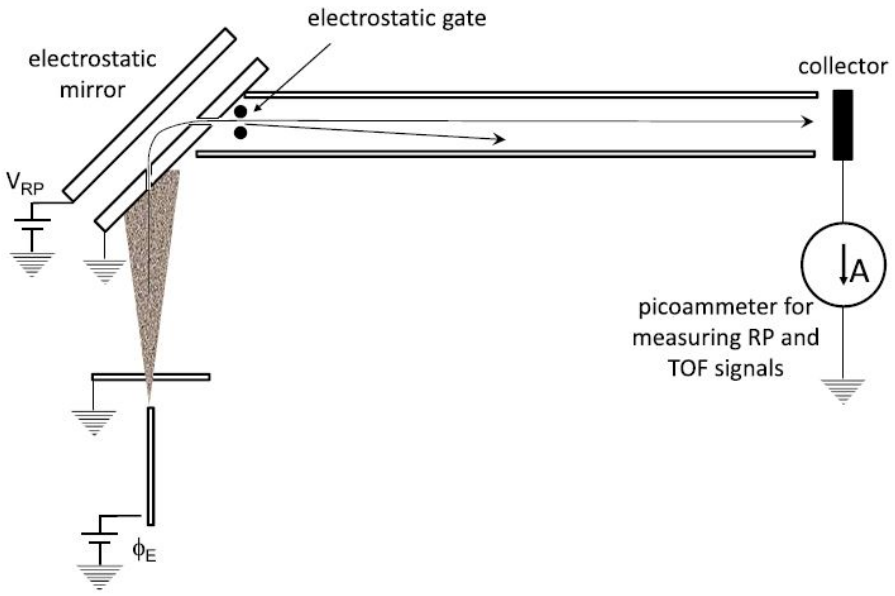

Figure 2.7: Retarding potential (electrostatic mirror) and time-of-flight analyzers operated in tandem.

velocity of the jet v_J and the potential of the jet at the breakup point ϕ_J through the linear regression of Eq. 2.32. During the free flight region droplets and ions are not affected by the electrostatic field induced by the electrodes, hence, all they have is potential energy. Since mechanical energy must be conserved, the kinetic energy of a particle at the free flight region must be equal to its retarding potential ϕ_{RPi} multiplied by its charge q_i

$$q_i \phi_{RPi} = \frac{1}{2} m_i v_i^2 \tag{2.33}$$

The time of flight measurement will give us the velocity of the particle

$$v_i = \frac{L_{TOF}}{\tau_{TOFi}} \tag{2.34}$$

which then yields an equation to calculate the charge-to-mass ratio distribution

$$\xi_i = \frac{L_{TOF}^2}{2\phi_{RPi}\tau_{TOFi}^2} \tag{2.35}$$

The drawback of such analysis is that it only samples a small region of the beam [22]. Since we knew from previous experiments that droplets would segregate according to their charge-to-mass ratio, we decided to use data that was sampling all the beam. We use a time-of-flight measurement of the full beam, together with the average value of the retarding potential, to estimate the density distribution $g(\xi)$ of Eq. 2.36. As an example, Fig. 2.8 shows the time-of-flight curve of an EMI-Im beam with a current of 305 nA [21]. The droplet and ion populations are easily separated by their very different velocities and times-of-flight, the ions representing 15.4 % of the total beam current. The average retarding potential of the droplet population is 1471 V, and the time-of-flight path is 0.147 m. When using these values in (2.35), the time-of-flight curve for the droplets is directly converted into the charge-to-mass ratio cumulative distribution shown in Figure 2.9, and into the density distribution $g(\xi)$ upon differentiation. For the purpose of numerical calculations, the distribution is discretized into a large number of bins, with the centers of the bins shown as red dots on the distribution curves.

Figure 2.9 has six bins marked with dots of different colors, these six representative groups will be used to analyze the results in Chapter 3.

The sequence of droplets needed for the inner solution must be representative of the variation of sizes and charge-to-mass ratios produced by the jet breakup. Although the resulting distributions have been measured for micron-sized and slightly smaller droplets [18], only partial experimental information is available for highly conducting propellants. In particular, the charge-to-mass ratios can be measured with the time-of-flight technique, but the diameters of such small droplets cannot be fully characterized. In the absence of detailed information, we assume the distribution

$$f(D,\xi) = \frac{g(\xi)}{\sigma\sqrt{2\pi}}\, e^{-\frac{1}{2}\left(\frac{D-D_c}{\sigma}\right)^2} \tag{2.36}$$

where $g(\xi)$ is obtained from time-of-flight experiments, and the mean of the normal distri-

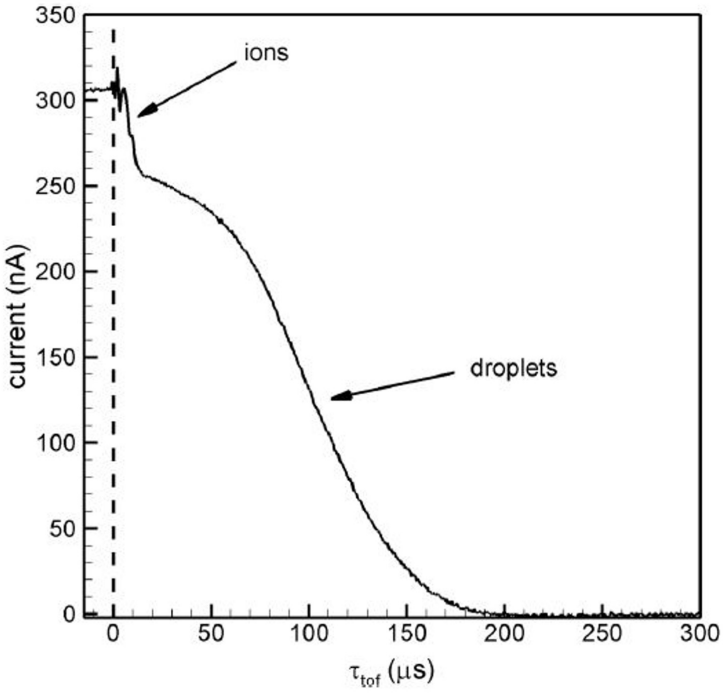

Figure 2.8: Time-of-flight curve for a full beam of EMI-Im.

bution depends on the charge-to-mass ratio, $D_c(\xi)$. In the calculations, we use a typical standard deviation σ of 10% of D_c. [53]

We use linear instability analysis of capillary breakup to estimate $D_c(\xi)$ [22]. The small electrical relaxation time of EMI-Im compared to characteristic breakup times makes the process quasi-electrostatic. Furthermore, these jets have very high values of the Ohnesorge and Taylor numbers (viscous diffusion is very efficient, and the electrostatic pressure is always large, in some cases exceeding the capillary pressure). Under such conditions the diameter D_{crit} of the most likely droplet produced by the breakup (i.e. the diameter with maximum growth rate derived from the instability analysis) is approximately given by [22]

$$\frac{D_{crit}}{D_J} \cong \left(\frac{9}{\Psi}\right)^{1/3}, \tag{2.37}$$

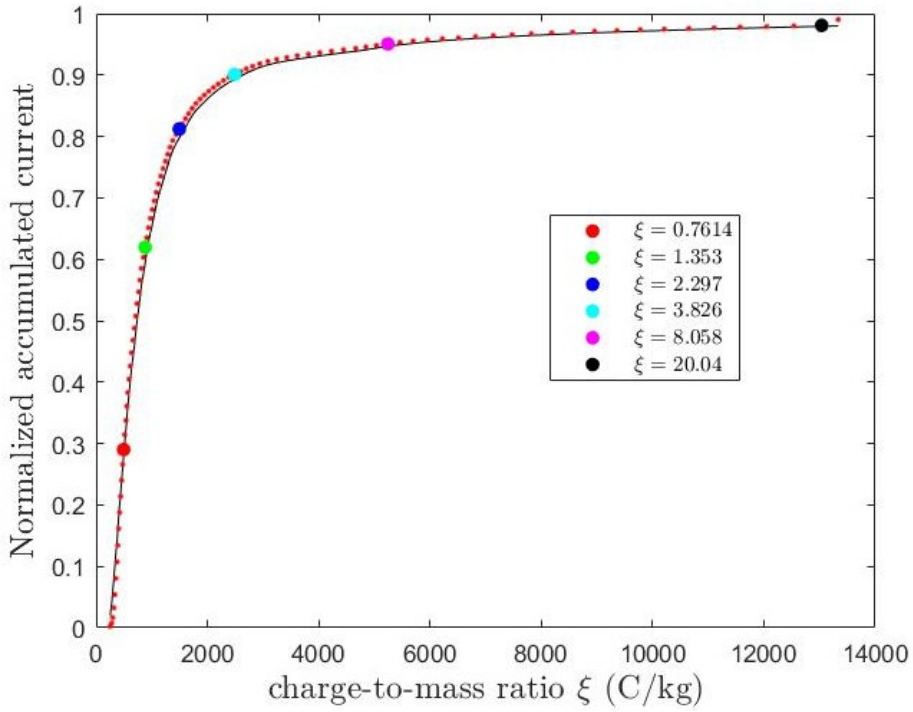

Figure 2.9: Numerical charge to mass ratio distribution

where the Taylor number is

$$\Psi = \frac{\varsigma^2 D_J}{2\varepsilon_0 \gamma} = \frac{{I_B}^2}{2\pi^2 \varepsilon_0 \gamma D_J {\mathrm{v}_J}^2}. \tag{2.38}$$

I_B, ς and γ stand for the beam current, surface charge density of the jet, and the surface tension of the liquid respectively. The charge-to-mass ratio of a droplet scales with the square of its diameter in an equipotential breakup. In addition, since conservation of charge and mass requires the average charge-to-mass ratio of the most likely droplet to be similar to that of the jet, we can approximate the sought mean diameter by:

$$D_c \cong D_{crit} \left(\frac{\xi}{\xi_J}\right)^{1/2} \cong \left(\frac{9}{\Psi}\right)^{1/3} D_J \left(\frac{\xi}{\xi_J}\right)^{1/2}. \tag{2.39}$$

Once the joint $f(D, \xi)$ distribution is determined, the sequence of droplets is constructed in two steps. First, we generate a large pool of droplets (typically 100,000) by sampling $f(D, \xi)$.

Second, subsets of droplets (typically 15) are randomly extracted from this pool, subject to the condition that their total charge is within a small fraction of that in a section of the jet with the same volume. Subsets that fulfill this condition are added to the sequence and removed from the pool. This ensures that the sequence of droplets fulfills conservation of charge at frequencies comparable to that of droplet emission. Since the net charge in the jet is distributed on its surface, and the electric current transported by the jet is the advection of this surface charge, the net charge contained in a section of the jet of length L is equal to $I_B L/\mathrm{v}_J$.[29]

The droplets are inserted sequentially in the computational domain at times $t_{o,i}$ fixed by conservation of mass:

$$t_{o,i} = t_{o,i-1} + \frac{{D_{i-1}}^3 + {D_i}^3}{3\mathrm{v}_J {D_J}^2}. \tag{2.40}$$

where D_i and D_J stand for the diameters of the i^{th} droplet and the jet at the breakup respectively.

Finally, to incorporate the jet's lateral oscillations on the initial conditions of the droplets we randomly set their initial positions within a circle of radius r_o centered on the axis (r_o should have a value of the order of the diameter of the jet), and use a random oscillation with maximum angle φ_o to distribute v_J among the three components of the initial velocity:

$$\boldsymbol{\alpha}_i = \begin{bmatrix} r_o A_i \cos\theta_i \\ r_o A_i \sin\theta_i \\ 0 \end{bmatrix} \quad , \quad \boldsymbol{\beta}_i = \begin{bmatrix} \mathrm{v}_J \sin(B_i \varphi_o)\cos\theta_i \\ \mathrm{v}_J \sin(B_i \varphi_o)\sin\theta_i \\ \mathrm{v}_J \cos(B_i \varphi_o) \end{bmatrix} \tag{2.41}$$

A_i and B_i are numbers picked randomly from a continuous uniform distribution between 0 and 1, and θ_i is an azimuthal angle picked randomly from a continuous uniform distribution between 0 and 2π. $\boldsymbol{\alpha}_i$ and $\boldsymbol{\beta}_i$ were introduced in equations (2.15) and (2.16).

2.3 Modelling of field emitted-ions

We use the continuum approach (2.24)-(2.26) to model the expansion of the ion beam. Retarding potential measurements show that the ions present in electrosprays of EMI-Im are emitted from droplets in flight within and immediately downstream of the breakup region, and possibly from the surface of the jet [22]. This bounds the initial positions of the trajectories. We divide the ion current into groups, each one simulating emission from a stationary droplet. These sources of ions are placed at regular intervals inside the beam of droplets and, based on retarding potential measurements, within a few hundred Volts from the breakup. We define $m \times n$ characteristics for each group, all starting at the position of the droplet source and with initial velocities simulating spherical and homogeneous emission

$$\dot{\mathbf{x}}_{p,q}(t_o) = \begin{bmatrix} \mathrm{v}_e \sin\left(\frac{\pi p}{m-1}\right) \cos\left(\frac{2\pi q}{n}\right) \\ \mathrm{v}_e \sin\left(\frac{\pi p}{m-1}\right) \sin\left(\frac{2\pi q}{n}\right) \\ \mathrm{v}_e \cos\left(\frac{\pi p}{m-1}\right) \end{bmatrix}$$
$$\text{with} \quad p = 0, 1, ..., m-1\,, \quad q = 0, 1, ..., n-1 \tag{2.42}$$

The modulus of the initial velocity is derived from the self-potential of the droplet,

$$\mathrm{v}_e = \sqrt{2\xi_{ion}\phi_{self}} \tag{2.43}$$

, with

$$\phi_{self} = q/\left(2\pi\varepsilon_0 D\right). \tag{2.44}$$

Since the breakup is nearly equipotential, the emission velocity is to first approximation independent of the diameter of the droplet. For an electrospray of EMI-Im with a current of 300 nA our estimates of the droplet self-potential and the ion emission velocity are $\phi_{self} = 19$

V and v_e = 2688 m/s. Ion emission from the jet can be simulated as an additional group with characteristics starting at the axis immediately upstream of the breakup point, and with a radial velocity derived from the self-potential of the jet.

2.4 Numerical algorithm

The flow chart in Fig. 2.10 shows the main steps in the algorithm used for solving the model.

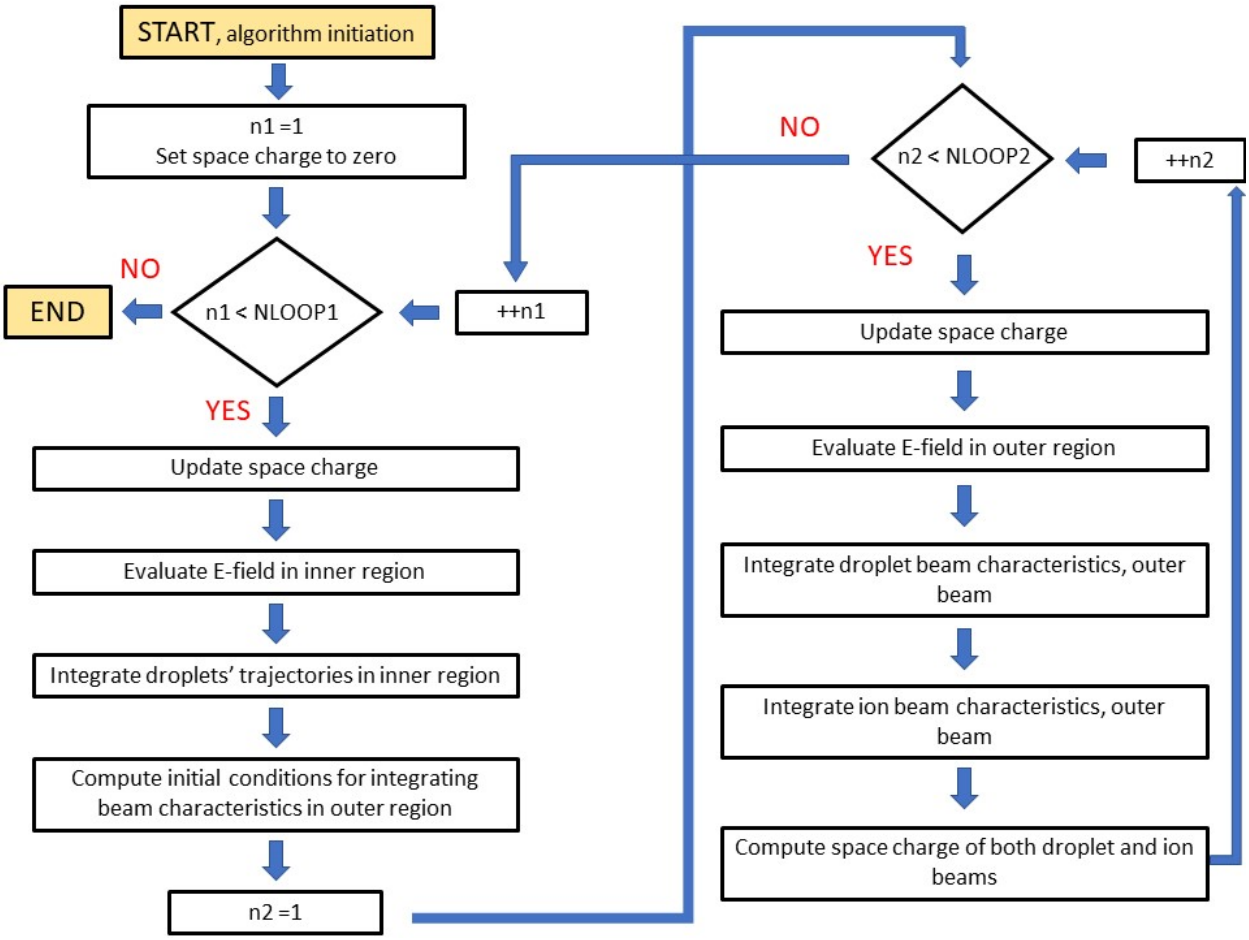

Figure 2.10: Algorithm for solving the model.

In an initial block we define basic inputs such as the beam current, emitter potential, temperature, domain geometry and boundary conditions; compute the dimensionless numbers

present in the equations, the sequence of droplets to fly and the break-up position of the jet; define the grids for discretizing the space charge and evaluating the axisymmetric electric field; and compute the matrices and vectors of constant coefficients needed for evaluating the electric field.

This is followed by integrating the trajectories of droplets in the inner region through the Störmer–Verlet method. The matrices needed for the calculation of the electric field have already been computed in the initial block, hence, at each time step only the space charge of each cell needs to be updated. Once the integration is complete, the position and velocity of droplets at the boundary are averaged and the initial conditions for the outer problem are computed. Then, the solution for the outer region is calculated. The droplet trajectories are obtained by integrating the equation of motion with the method of the characteristics using a fourth-order Runge-Kutta scheme with variable timestep. Finally, the characteristics of the ion beam are obtained using the same integrating scheme.

Notice that in this first iteration, solutions have been computed assuming a domain empty of space charge. Therefore, it is necessary to do a few more iterations with the updated space charge to obtain an accurate solution. There is a main loop where the inner solution is computed and processed to determine the initial conditions for the outer region; and an inner loop in which the outer region is solved. In both the main and inner loops the space charge is updated with the latest available solution, and the electric field is reevaluated with this information. Following this scheme allows simulating the emission of an electrospray within a reasonable computational time without compromising accuracy. The space charge in the outer region affects the solution of the inner region and the solution of the outer region too. The differences between the first iteration and the second one are not very large, only a few degrees in the trajectories. It will be shown in Chapter 3 that this is because the effect of the space charge is really important at the emission point but its contribution decreases

along the axial direction due to the reduction in droplet and ion densities. However, it still has an effect and that is why the second iteration must be done. The third and final iteration is already very similar to the second one.

The last block of the model processes the data and extracts information from the solution obtained.

.

Chapter 3

Analysis of the Numerical Solution

Chapter 3 presents the results obtained with the model described in Chapter 1 applied to the microfabricated electrospray source developed in our group [7]. One single emitter does not produce enough thrust to be used as a primary propulsion system for spacecraft. To achieve higher levels of thrust, hundreds or thousands of emitters need to operate simultaneously. Arrays of emitters that can fit small spacecraft's size and mass constraints can only be produced through MEMS techniques. Tools from the semiconductor industry are used to carve emitters in silicon wafers. Once the process is developed and optimized, arrays of emitters can be produced at a low-cost in a highly scalable environment, making this manufacturing technique very suitable to fulfill the demand of propulsion systems for the commercial space. The detailed process on how these microfabricated electrospray sourced are manufactured and operated will not be presented in this report, instead, the focus will be on the validation of the proposed geometry and the study on how this geometry affects the emission. Understanding how the beam will expand within the region between the emitter electrode and the extractor electrode is extremely important. Beam interception at the extracting electrode is the primary limiting factor of electrospray thrusters [63]. Either the extracting electrode will erode over time or the progressive accumulation of propellant will

ultimately lead to the shorting of the emitter and extractor electrodes. The challenge arises while trying to pack emitters in high densities. Each emitter needs a perfectly aligned orifice in the extracting electrode to let the beam go through, hence, if the emitters are closer to each other, the orifices on the extracting electrode have to be smaller too. Figure 3.1 shows both sides of two extracting electrodes, one for an array of 64 emitters and the other for an array of 256 emitters. Just by looking at the figure, it can be seen clearly that the diameter of the extracting orifices will have to be smaller to increase the density of emitters.

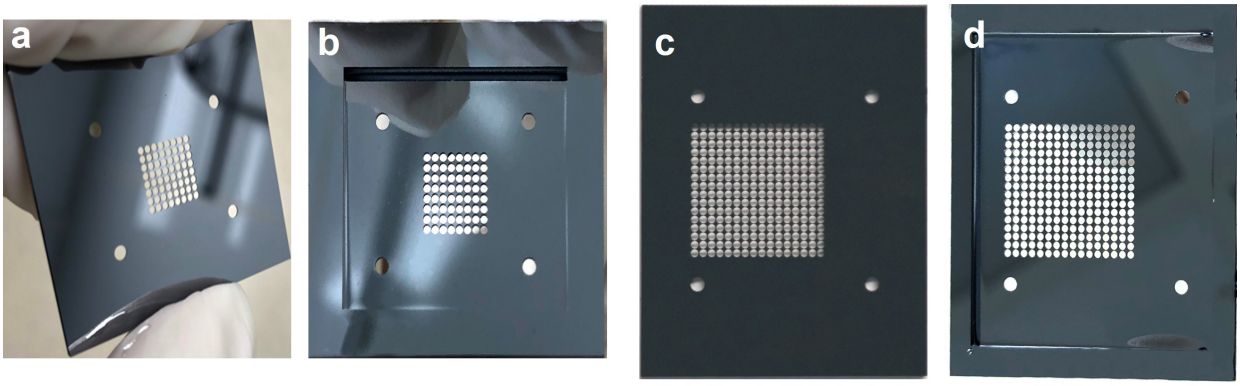

Figure 3.1: a) topside of the extractor electrode for the 64 emitter source; b) backside of the extractor electrode for the 64 emitter source; c) topside of the extractor for the 256 emitter source; d) backside of the extractor for the 256 emitter source.

Figure 3.2a. shows a schematic drawing with the characteristic dimensions of the MEMS electrospray source and Figure 3.2b. shows an SEM picture of two microfabricated emitters part of a 256 electrospray sources facing the extractor electrode with the dimensions described.

Each emitter is a cylindrical tube formed by etching a surrounding well and an axial, circular conduit. The diameter of the well is 900 μm, and the pitch between emitters is 1 mm. The height, outer diameter and inner diameter of the emitters are 275 μm, 100 μm and 40 μm respectively. The extractor electrode has a square array of extractor orifices, matching and perfectly centered with the square array of emitters. Each orifice has a diameter of 0.9 mm

and the gap between extractor electrode and emitter electrode is 250 μm.

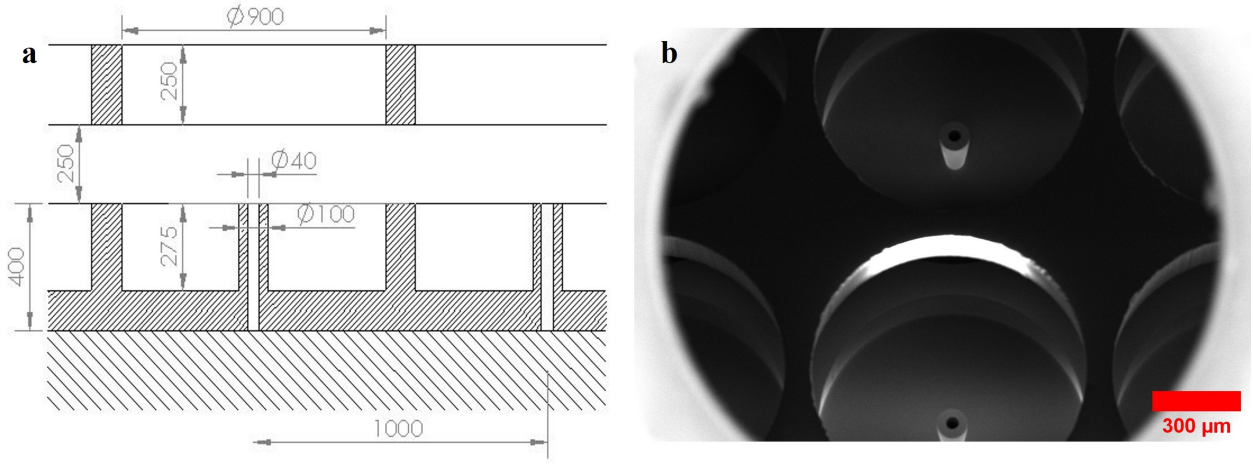

Figure 3.2: a) Cross section of the micromachined electrospray source showing the dimensions of an emitter and the extractor. Dimensions in μm b) SEM image of two microfabricated emitters, part of a 256 emitter arrray, aligned with the extractor electrode.

The results presented below correspond to an EMI-Im beam of 300nA. The emitter electrode is fixed at 1690V and the extracting electrode is grounded. A maximum jet oscillation angle $\varphi_{max} = 14.75$ deg and an emission circle with $r_o/D_J = 5.7$ are used to set the initial conditions (Section 3.3 will show that these choices yield the best comparison with experiments).

3.1 Inner region

Figure 3.3 shows the fraction of the current that exits the inner region below a given polar angle for six representative droplet groups. Although the segregation of droplets by charge-to-mass ratios is evident (the higher the charge-to-mass ratio the larger the exit polar angle at a current fraction of 50%), the droplet groups overlap significantly. This is caused because of the strong radial electric field induced by the high space charge density at the emission point. Droplets that have a higher charge-to-mass ratio are more sensitive to the effect of the electric field and suffer from stronger deflection. On the other side, bigger and slower droplets

have more inertia and are less affected by the Coulomb interactions between particles, hence, the deflection is less severe and they stay closer to the axis. There is also a segregation of droplets by sizes, with smaller droplets preferentially moving farther away from the axis.

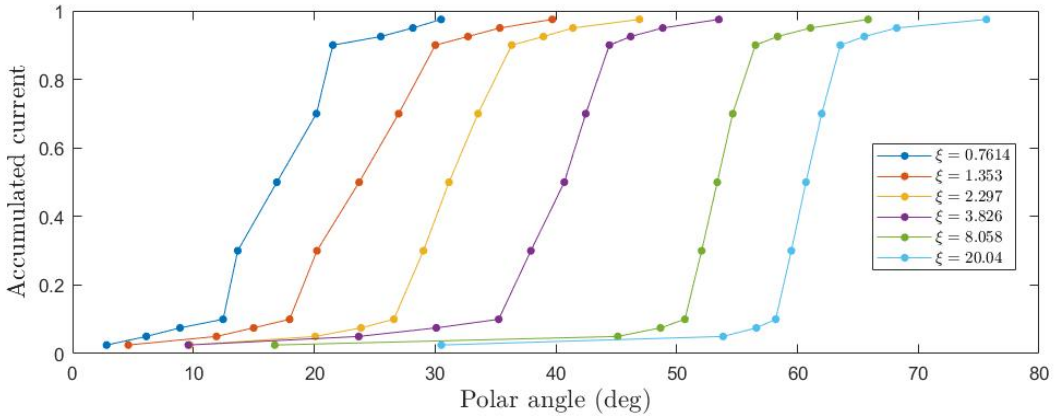

Figure 3.3: Envelopes' accumulated current of six representative groups of charge-to-mass ratio (normalized with $\xi_J = 650.582\ C\,kg^{-1}$) as a function of the polar angle.

Once the droplets cross the boundary between the inner and outer regions they are removed from the integration, and their exit positions and velocities are averaged to obtain the initial conditions for the outer problem. The average exit velocities of six representative droplet groups are illustrated in Figure 3.4 with vectors spanning the full exit range of each group (11 vectors for each group). Each vector is marked in Figure 3.3 as a dot for comparison.

Figure Fig. 3.5 shows the angle formed by the components of the average exit velocities. This angle depends on the exit position and is independent of the charge-to-mass ratio, matching the polar angle up to approximately $\varphi = 28$ deg, and falling below for higher values.

The electric field determines the trajectories of the droplets. Figures 3.6 and 3.7 analyze its radial component in the inner region, which is key for the expansion of the beam. The axial component is mostly determined by the electrodes, and is approximately constant within this small region.

Figure 3.6 shows the electric field induced by the space charge normalized with its maximum

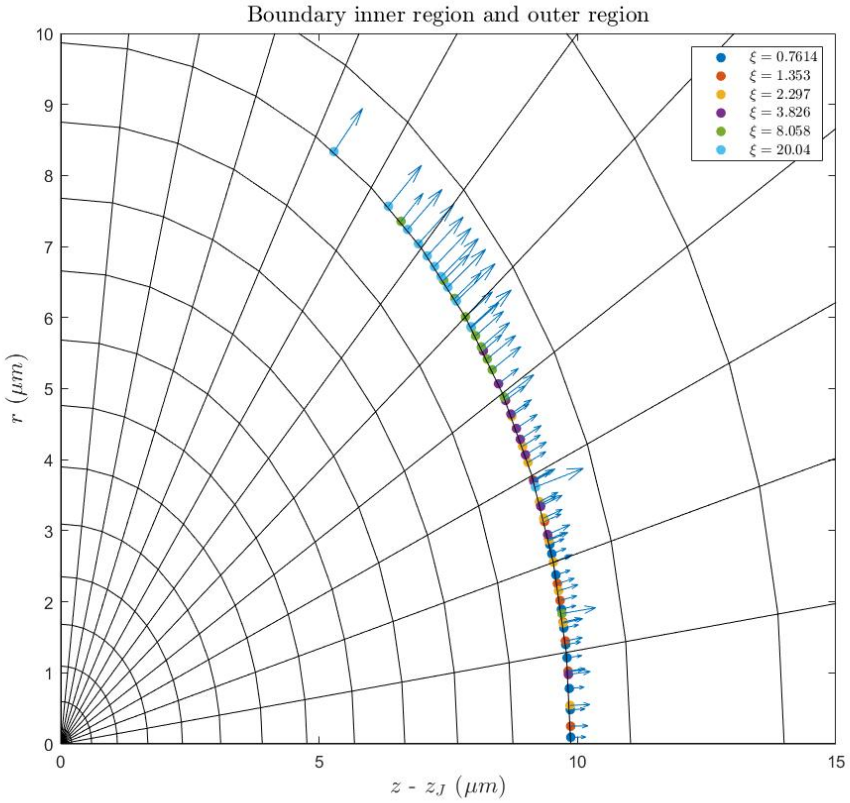

Figure 3.4: Averaged position and velocities of six representative groups of charge-to-mass ratio (normalized with $\xi_J = 650.582\, C\, kg^{-1}$) at the boundary between the inner region and the outer region.

value (38087 V/mm). The direct contribution from neighboring droplets is important only within a small zone near the emission point and decays rapidly away from it. Thus, although repulsion between charged droplets is key for the expansion of the beam, direct droplet-on-droplet interactions only need to be retained within a few microns from the emission point. Elsewhere the continuum treatment of the space charge is an excellent approximation.

Figure 3.7 shows the radial electric field induced by the electrodes normalized with the maximum electric field induced by the space charge (38087 V/mm), which is obtained from solving the Laplace equation

$$\nabla^2 \phi = 0 \tag{3.1}$$

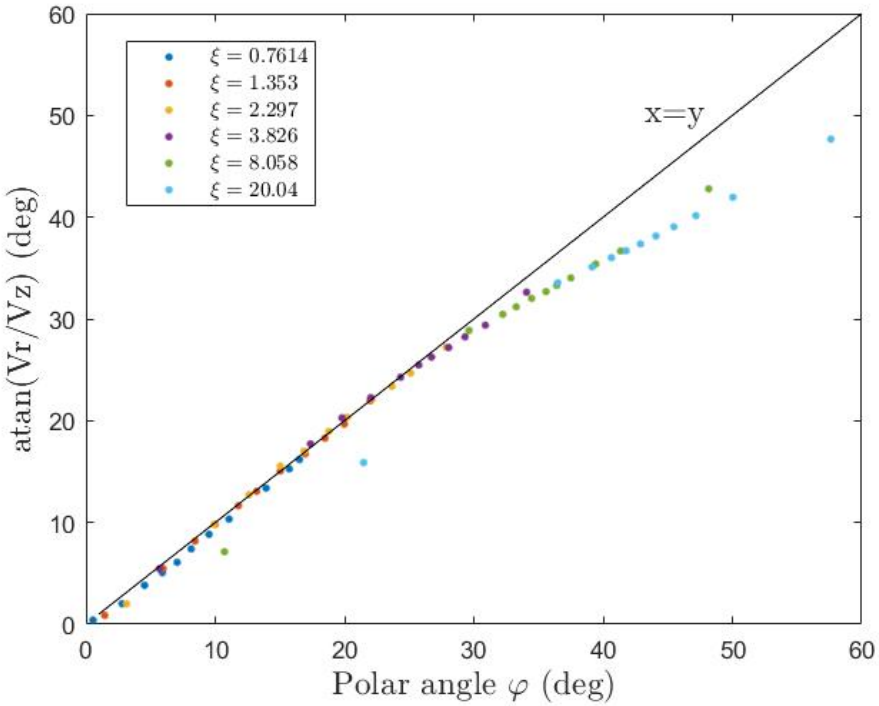

Figure 3.5: Velocity vector angle of six representative groups of charge-to-mass ratio (normalized with $\xi_J = 650.582\ C\,kg^{-1}$) at the boundary between the inner region and the outer region as a function of the polar angle.

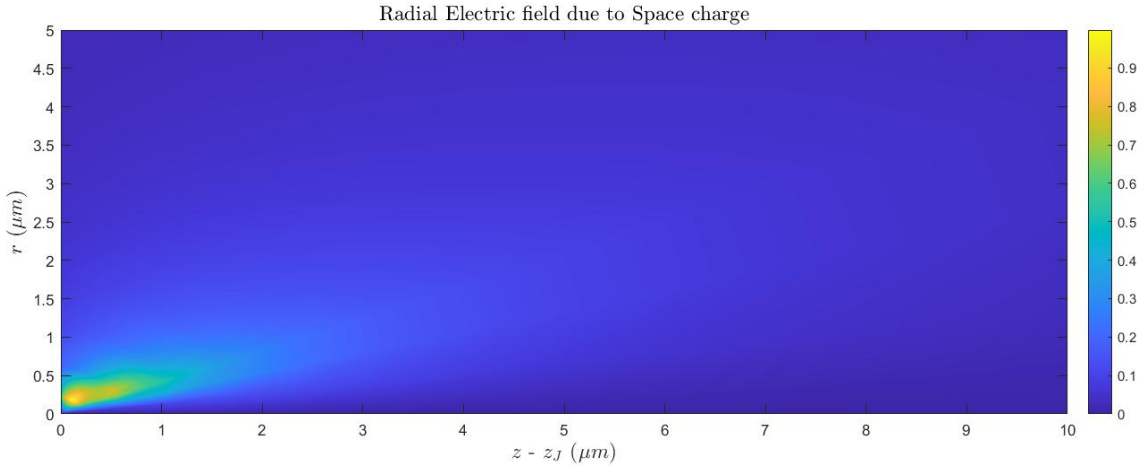

Figure 3.6: Radial electric field induced by the space charge normalized with its maximum value (38087 V/mm)

and computing the gradient in the radial direction. We can see that the contribution of the electrodes to the radial electric field is very small, which means that the divergence of the beam is caused by the space charge and the initial velocities distribution associated with the

oscillations of the jet. In the absence of space charge the field would decrease monotonically to zero towards the axis, but when there is a beam of charged particles the space charge induces a radial electric field that peaks near the axis, and is most intense near the emission region.

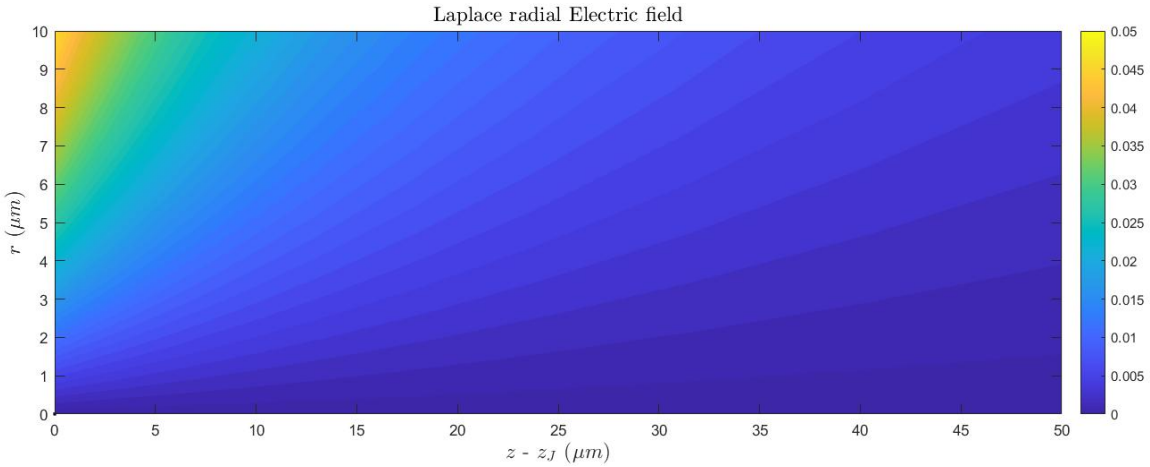

Figure 3.7: Radial electric field induced by the electrodes normalized with the maximum electric field induced by the space charge (38087 V/mm)

3.2 Outer region

Figure 3.8 shows three characteristic curves, i.e the trajectories, for six representative groups of charge-to-mass ratio. These representative groups have been defined according to the accumulated current that they carry, which can be seen in Figure 2.9. The marks on the lines indicate the fraction of the current of the group that is enclosed in each characteristic curve. The line with a triangle pointing upwards contains 98% of the current, and the one pointing to the right and the one pointing downwards contain 50% and 5% respectively.

Droplets spread according to their charge-to-mass ratio due to the repulsion caused by Coulomb interaction near the emission point. Such interaction is captured by the inner region's solution and extended to the outer region. The strong axial field induced by the

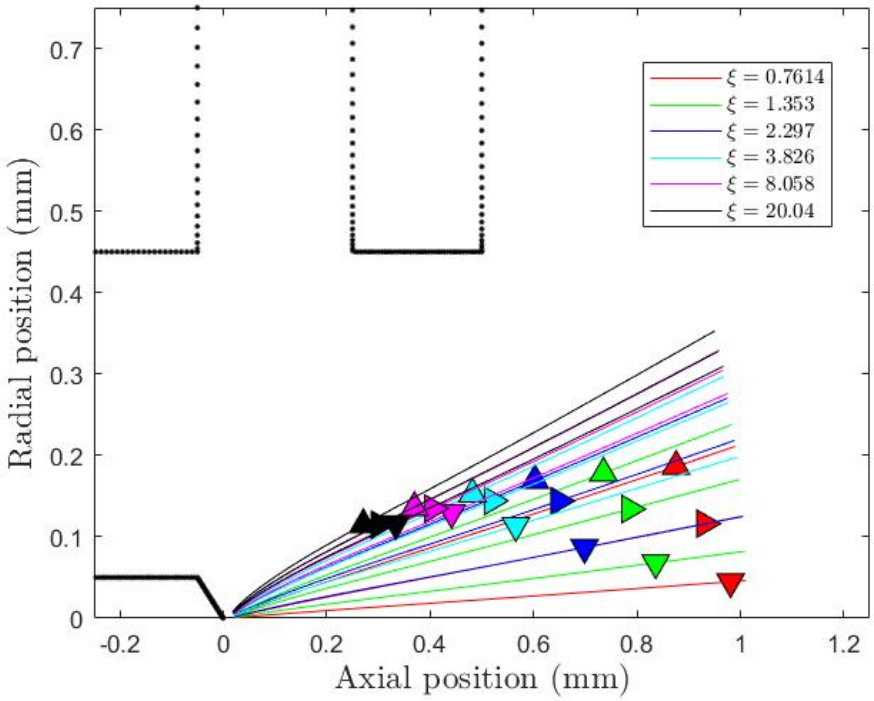

Figure 3.8: a) Envelopes containing 98%, 50% and 5% of the current of six representative groups with different charge-to-mass ratio (normalized with $\xi_J = 650.582\, C\, kg^{-1}$). Triangle pointing upwards, to the right and downwards, respectively.

electrodes dominates over the radial electric field and slightly focuses the beam. The axial velocity increases at a higher rate than the radial velocity, thus reducing the local angle of the velocity θ, which is defined as the angle formed by the axial and radial velocities

$$\theta = atan\left(\frac{V_r}{V_z}\right) \tag{3.2}$$

. This effect benefits the most droplets with a higher charge-to-mass ratio since they are more sensitive to the electric field and deflect the most, e.g., the characteristics for $\xi/\xi_J = 20.4$ reduce their polar angle to half its initial value whereas the characteristics for $\xi/\xi_J = 0.761$ only reduce it by a few degrees. Even if the polar angle is considerably reduced, it still has a significant value, causing droplets to keep spreading in space.

The characteristics do not intersect because the electric field in the outer region, mostly the result of the potential difference and the geometry of the electrodes, does not have a strong focusing effect. For example, a three-electrode geometry would significantly increase the focusing effect of the electrodes and would cause the characteristics to intersect.

In Figure 3.9 we can see that the higher the charge-to-mass ratio the closer the three characteristics are to each other, which means that most of the current carried by faster droplets is contained within a narrow range of local angles. For example, if we look at the envelope enclosing the current carried by the family with a charge-to-mass ratio of $\xi/\xi_J = 20.4$, we can see that 93% of the current is contained within 2.4^{o} but if we look at the family with a charge-to-mass ratio of $\xi/\xi_J = 0.7614$, we can see that the same fraction of current is contained within 10.5^{o}.

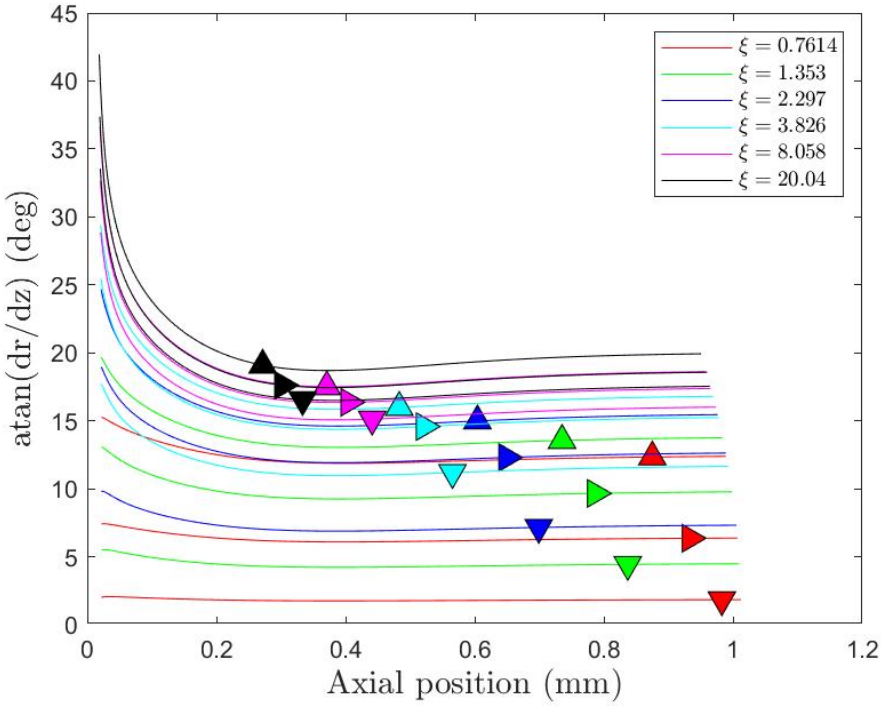

Figure 3.9: Velocity angle θ of the characteristics

Droplets with a higher charge-to-mass ratio undergo a stronger acceleration and achieve higher velocities. Figure 3.10a shows the total velocity of the six representative groups

of charge-to-mass ratio along the axis and Figure 3.10b shows only the radial component. Droplets with $\xi/\xi_J = 20.4$ are ten times faster than $\xi/\xi_J = 0.7614$. It is also interesting to notice that the total velocity curves of all envelopes for a particular group of charge-to-mass ratio collapse in one unique curve whereas the curves for the radial velocity component do not. That means that within a group of charge-to-mass ratio, droplets closer to the axis have higher axial velocity.

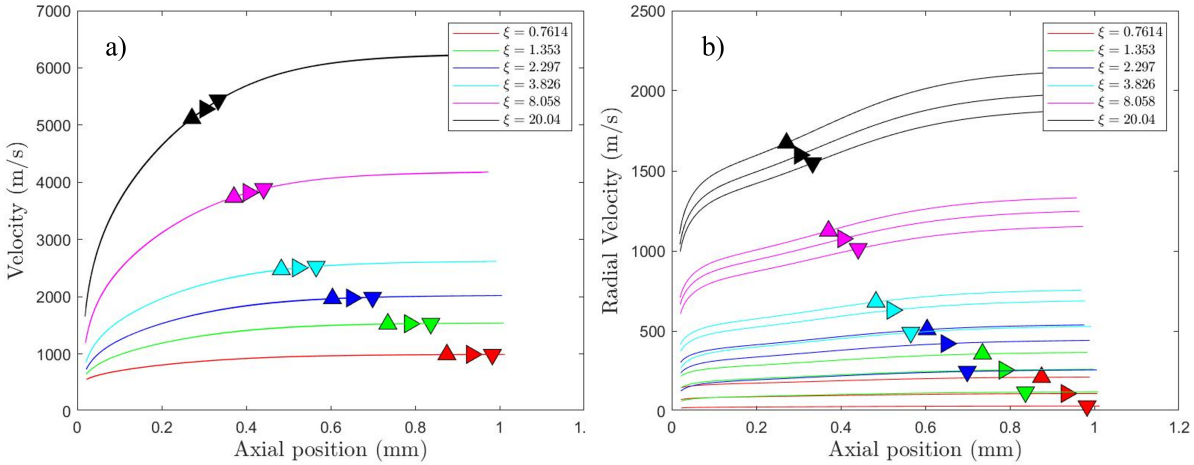

Figure 3.10: a) total velocity and b) radial velocity of six representative groups of charge-to-mass ratio along the axis.

Figure 3.11 shows the characteristics of the ion beam. We consider emission from droplets in flight, as well as from the surface of the jet upstream of the breakup.

Two results are most significant: first, if ions were emitted from the jet just upstream of the breakup, they would be narrowly distributed and concentrated in the outer region of the beam of droplets, enveloping it. Thus, if a significant fraction of the ion current were emitted from the jet, the beam current profiles would display a strong and narrow local maximum at the largest polar angles of its range. This is not observed in experiments with EMI-Im, which instead show that ions appear throughout the beam, down to its axis [19, 21, 58]. On the basis of this comparison, we conclude that there is not significant emission of ions from the surface of the jet in EMI-Im electrosprays. Second, the characteristics of ions emitted from droplets

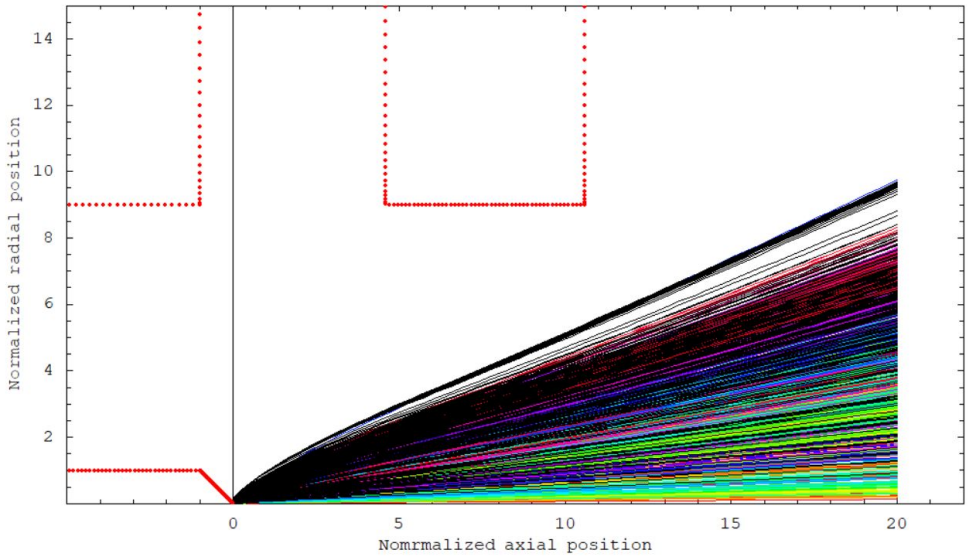

Figure 3.11: Characteristic lines of the ions trajectories, in black. Characteristic lines of the trajectories of droplets, in colours.

in flight overlap with the droplet beam, in agreement with experiments. This may seem to contradict the segregation of droplets by charge-to-mass ratios, which if extrapolated to the ions would make them appear fully separated from the droplets, enveloping them. However, the emission of ions and the subsequent interaction with charged particles is markedly different: droplets are emitted with a large kinetic energy per unit charge, mostly directed along the axis, and near the emission region repel away from other droplets with similar velocities. In these scattering events, the droplets with lower inertia and higher specific charge undergo the higher deflections, giving rise to angular segregation. On the other hand ions are evaporated from droplets in flight in every direction (including towards the axis and backwards towards the emitter), with similar initial speeds. Furthermore, Coulomb collisions between ions and droplets are not only unlikely (the droplet number density decreases rapidly downstream of the breakup), but also weak: in addition to the initial emission speed (associated with the droplet's self-potential of few tens of Volts), the ion gains significant kinetic energy during its flight in the potential field, before potentially flying near a second droplet. Thus, if the impact parameter is smaller than the radius of the droplet, the ion simply penetrates the droplet disappearing from the beam; otherwise its trajectory only suffers a slight deflection.

In summary, an ion only undergoes a significant "scattering event", i.e. the repulsion by the droplet from which it is emitted, which sends it into the beam with a significant velocity and in any possible direction. From this point on the interaction with other charged particles in the beam is well approximated by the interaction with a continuous space charge field.

3.3 Emission area and oscillating angle

In addition to the velocity of the fluid and the position of the jet breakup obtained from experiments, small radial displacements and radial velocity components must be specified to fully define the initial conditions of droplets. In the absence of a numerical solution of the breakup dynamics, we rely on (2.41) which randomly sets these values as functions of two parameters, r_o and φ_o.

We compare experimental measurements with numerical solutions for different values of r_o and φ_o to determine the effect of these two parameters on the expansion of the beam, and to find optimum values. The beam profile for our microfabricated electrospray thruster has not been measured yet, hence, it cannot be compared to the numerical result. The optimal values for r_o and φ_o were determined by comparing the beam profile of a single emitter source [21] and the numerical solution obtained using the same geometry [23]. The propellant, accelerating voltage, and beam current are the same as what we used for the results presented in the previous sections: EMI-Im; 1690V; and 300nA.

Figure 3.12 plots the root mean square of the difference between the experimental and computed accumulated current profiles:

$$I_{acc,rms} = \sqrt{\frac{1}{\pi}\int_0^{\pi}\left(\frac{I_{acc}(\varphi;model) - I_{acc}(\varphi;exp)}{I_B}\right)^2 d\varphi}, \tag{3.3}$$

for values of r_o/D_J and φ_o between 1 and 6.57, and 2 deg and 15.25 deg. The accumulated current $I_{acc}(\varphi)$ is the current transported by the beam between the axis and the polar angle φ. The difference is maximum for the smallest values of r_o and φ_o, and minimum for $r_o/D_J = 5.7$ and $\varphi_o = 14.7$ deg. It is worth noting that the optimum values are not unphysical: $r_o/D_J = 5.7$ means that droplets are emitted from within a circle with a radius that is 5.2 times the radius of the critical droplet, while $\varphi_o = 14.7$ deg indicates that the section of the jet that is oscillating is approximately a tenth of the estimated total length.

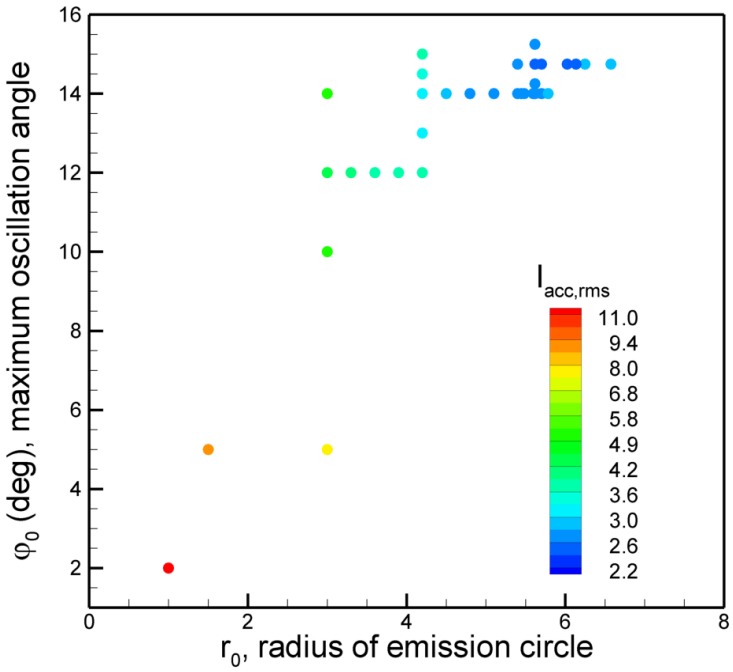

Figure 3.12: Error between experimental and computed accumulated current profiles, eq. (3.3), as a function of the radius r_o of the droplet emission circle and the maximum oscillation angle φ_o.

Figure 3.13 compares the experimental current profile with model results for several values of r_o and φ_o. The profiles are shown in both accumulated current form, figures (a) and (b), and in current density J form, figures (c) and (d):

$$J = \frac{1}{2\pi r^2 sin\varphi}\frac{dI_{acc}}{d\varphi}. \tag{3.4}$$

We plot $r^2 J$ for easier comparison at arbitrary distance from the emitter. The effect of the size of the emission area on the spreading of the beam is stronger at intermediate and large angles, and it does not significantly change the profile near the axis (compare curves with $\varphi_o = 5$ deg and emission radii of 3 and 1.5 in figures 3.13.a and 3.13.c). The oscillation angle has the opposite effect, changes on φ_o only affect significantly the profiles at small and intermediate angles (compare curves with $r_o/D_J = 3$ and oscillation angles of 10 and 5 deg in figures 3.13.a and 3.13.c). These dependencies of the beam structure are related to the angular segregation of droplets by size: the smaller the emission area the higher the initial Coulomb repulsion between droplets, which has a larger effect on small droplets (they have less inertia and their higher charge-to-mass ratios make them more sensitive to the electric field), and preferentially pushes them outwards. On the other hand the larger droplets are less affected by Coulomb repulsion, and need an initial radial velocity component to move away from the axis. Figures 3.13.b and 3.13.d show how the optimal values $r_o/D_J = 5.7$ and $\varphi_o = 14.7$ deg produce a solution that matches well the measured profile. Figures 3.13.b and 3.13.d also show the profiles of the droplet and ion beams for this optimal case, as well as the profile for values of the emission area and oscillation angle far from the optimum ($r_o/D_J = 1$ and $\varphi_o = 2$ deg). In the simulations all ions are emitted from droplets in flight, resulting in a beam with an angular range similar to that of the droplet beam.

3.4 Study at different flow rates

It has been observed experimentally that the beam profile gets wider as the flow rate, i.e. the beam current, increases [18, 21] and the model captures such effect.

Figure 3.14 shows the final local angle of the envelope containing all the current of each group of charge-to-mass ratio for different values of beam current. We can see that the beam gets wider as the beam current increases since all groups show a larger polar angle for a

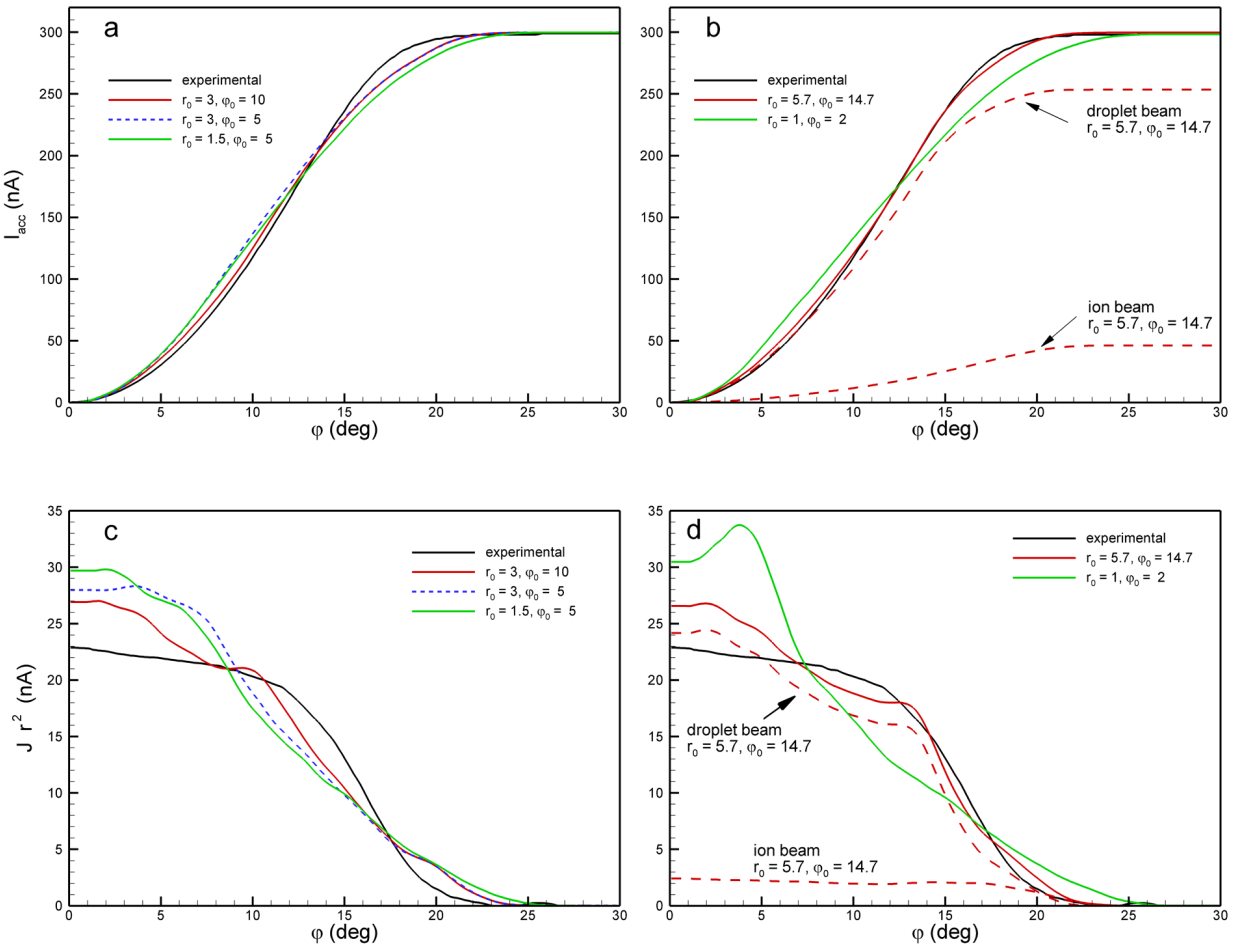

Figure 3.13: Experimental and computed accumulated current and current density profiles as a function of the polar angle with the beam axis: effects of the emission area and oscillation angle on the solution in (a) accumulated current representation, and (c) current density representation; profiles for optimal and poor values of r_o and φ_o in (b) accumulated current representation, and (d) current density representation. r_o is normalized with the diameter of the jet, $D_J = 27.7$ nm.

higher current.

This behavior occurs because the space charge at the emission point increases with the current of the beam, hence, the initial repulsion between droplets is higher and extrapolates to the rest of the beam.

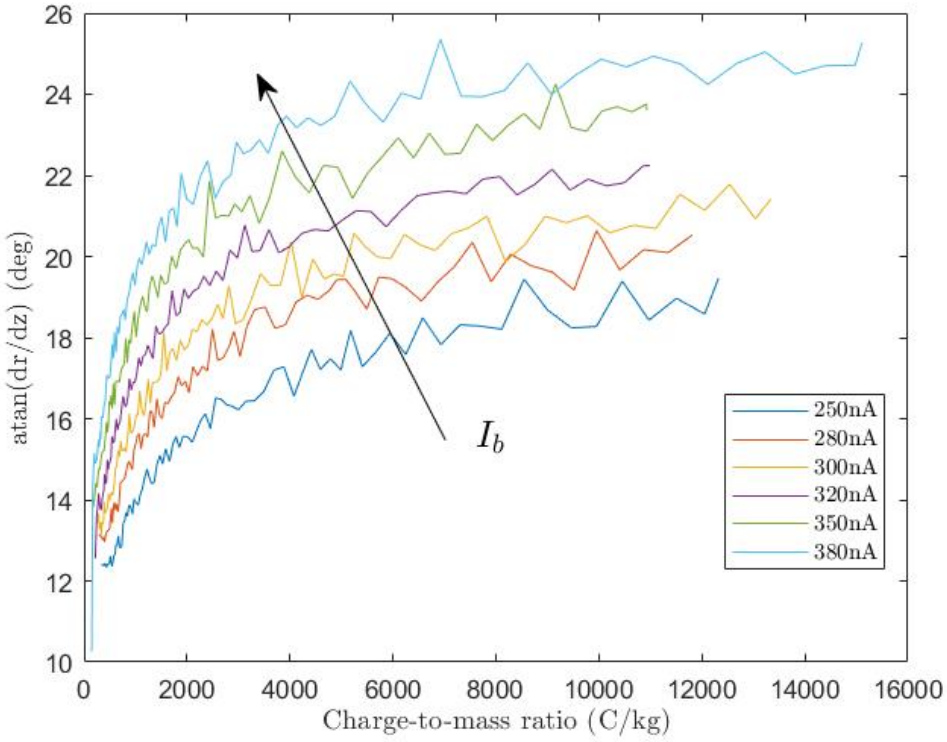

Figure 3.14: Final velocity angle of the envelope containing all the current of each group of charge-to-mass ratio for different values of beam

This phenomenon is better illustrated by presenting the accumulated current below a given polar angle, i.e. the beam profile, and its derivative. Figure 3.15 shows the beam profiles at different beam currents. Any given curve starts following a universal trend (initially parabolic) which continues for most of its polar angle range, and finally reaches asymptotes to a constant value. We can see that the polar angle at which the curve achieves the asymptote increases with the beam current. A beam of 380nA is fully enclosed in an envelope of approximately 25^{o} whereas the envelope enclosing a beam of 280nA is narrower, with a polar angle of 18^{o}.

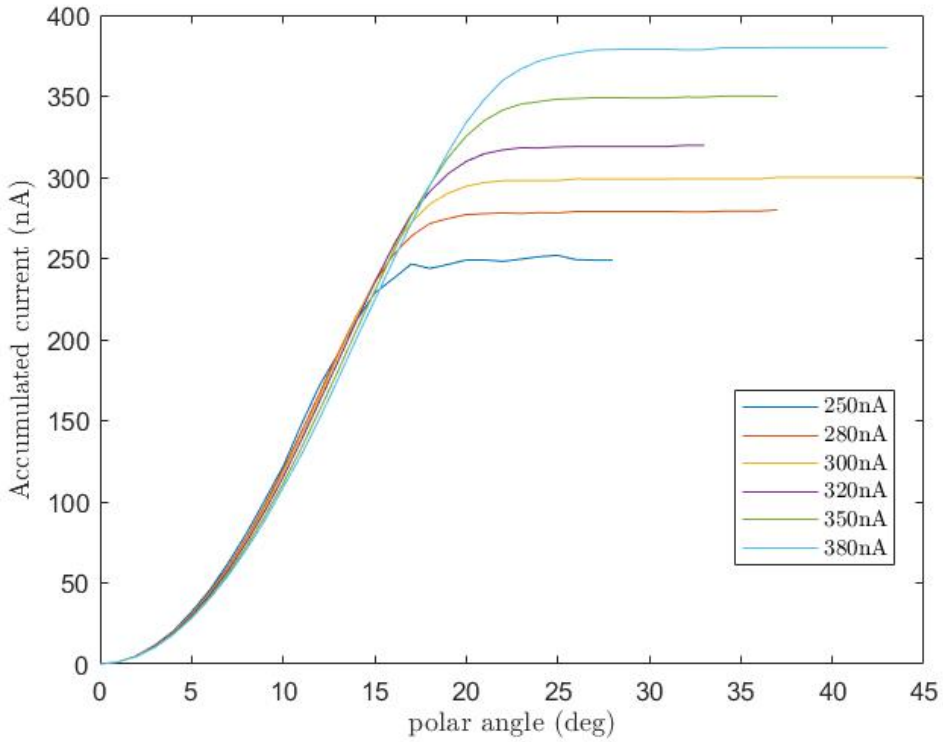

Figure 3.15: Accumulated current (nA) below a given polar angle φ

Figure 3.16 illustrates the derivative of the accumulated current with respect to the polar angle φ. In the region closer to the axis, the accumulated current is unaffected by the beam current. For polar angles up to approximately 10^{o}, all curves exhibit a similar pattern. This behavior can be attributed to the presence of slower and larger droplets near the beam's axis. These droplets are less influenced by the electric field resulting from the space charge and tend to remain close to the axis regardless of the beam current.

Conversely, curves associated with higher beam currents peak and remain positive at larger polar angles. This indicates that the accumulated current of the beam continues to increase as the polar angle increases, i.e. the beam gets wider as the beam current increases.

If we look at the dimensionless numbers of the problem, presented in Figure 3.17, we can see that the dimensionless number associated with the electric field induced by the space

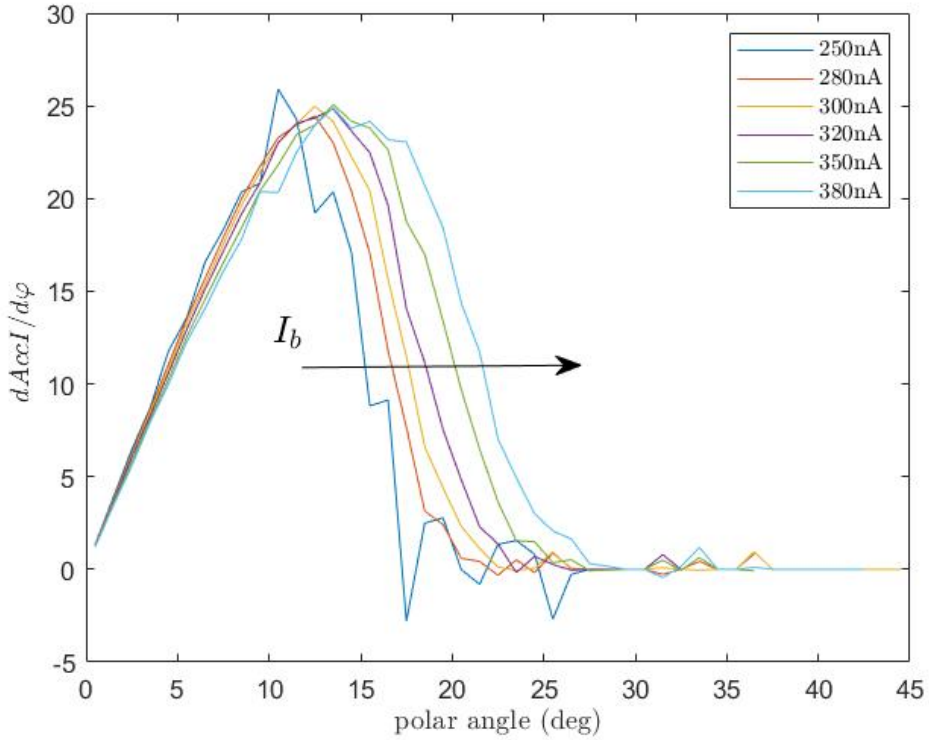

Figure 3.16: Derivative of the accumulated current (nA/deg) with respect to the polar angle φ

charge π_c increases with beam current whereas the dimensionless number associated with the electric field induced by the electrodes π_{XT} decreases. Figure 3.17 shows the tendency of π_c and π_{XT} as a function of the beam current.

Although Figure 3.15 shows that the beam gets wider with the current of the beam, droplets do not spread enough to intercept the extractor. The angle at which the model would start showing interception with the extractor in this geometry is 41.9^{o} and all beam profiles reach the asymptote before that.

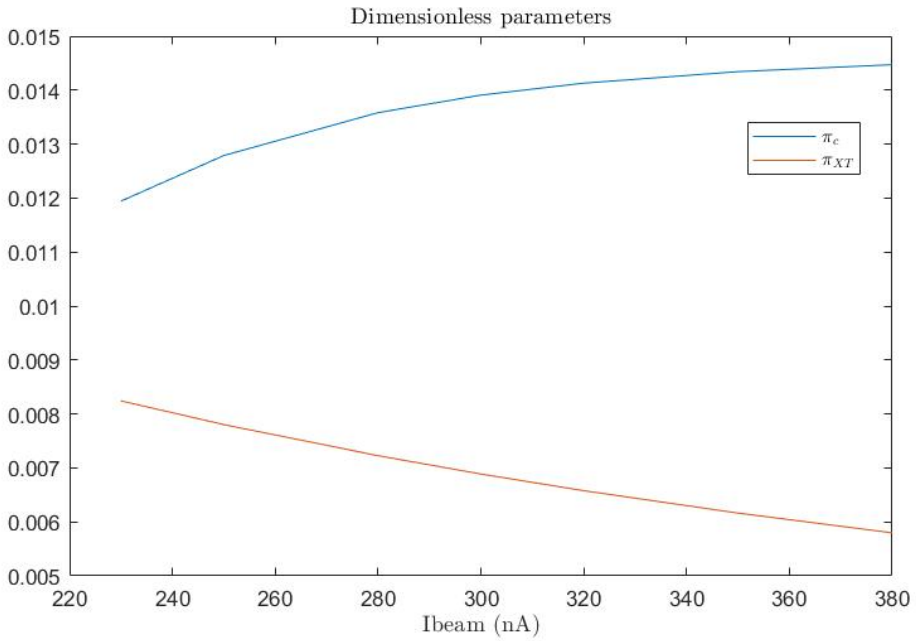

Figure 3.17: Dimensionless numbers of the problem as a function of the beam current

3.5 Comparison with experimental results

During the source's testing and characterization, we observed minimal impingement on the extractor [7]. The electrospray was operating between 40 μA and 70 μA, depending on the flow rate, and the intercepted current was always less than 0.25 μA, as it can be seen in Figure 3.18, which means that the interception is always less than 0.6%. Experimental measures have shown that the beam of EMI-Im gets broader as the beam current increases [18, 21], and our model reflects that. An explanation for the shape of the intercepted current shown in Figure 3.18 is that while the electrospray emitters are being operated at a lower flow rate, i.e., lower beam current, the beam is narrow, and the possible positive intercepted current is surpassed by the negative current coming from secondary emissions of the facility and by increasing the flow rate, the beam gets wider, and the difference between positive and negative current diminishes. Nevertheless, the model does not show interception with the extractor in any of the simulated cases. The disagreement between experimental and simulated results could be caused by a misalignment between the emitters and the extractor

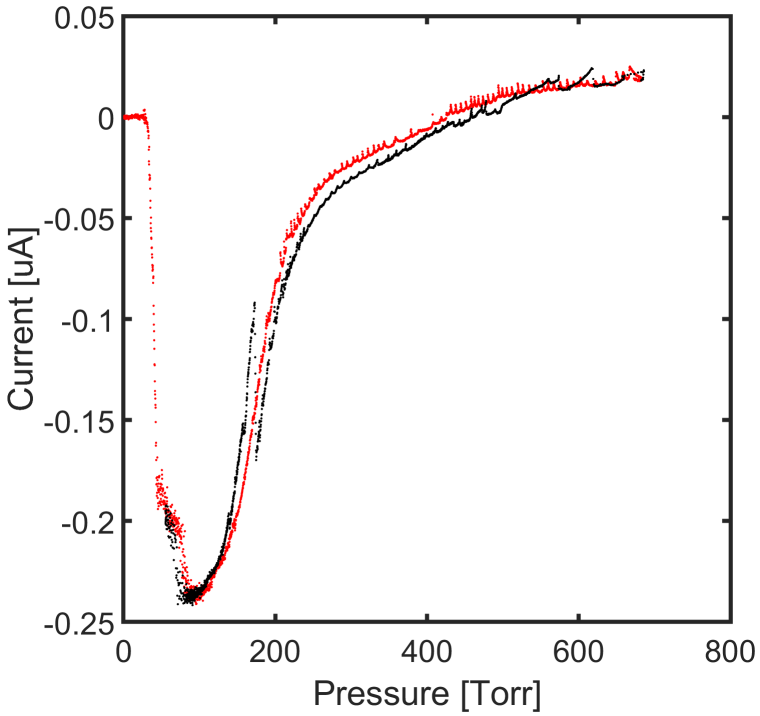

Figure 3.18: Measured intercepted current with the extracting electrode during the testing of the micromachined electrospray source

orifices of the micromachined electrospray source, by other effects related to secondary emissions and ground testing problems or by an unknown phenomenon that is not included in the beam model. In any case, further studies are required to reach a conclusion. Measuring the intercepted current is challenging due to the very low currents that need to be measured and all the facility effects produced during the testing, like secondary emission or backspraying from deposited films [59].

3.6 Focusing effect of the electrodes

We have seen that the electric field induced by the electrodes is what focuses the beam, in order to illustrate the effect that it has we have carried out the simulation varying the potential of the emitter electrode. Figure 3.19 shows the envelopes containing 98% of the current of the family with the highest charge-to-mass ratio ($\xi = 13037.66328\ C\,kg^{-1}$) for

different emitter potential values V_E. Section 3.1 shows that droplets segregate according to their charge-to-mass ratio because of the Coulombic repulsion occurring during the very beginning of the emission. Droplets with a higher charge-to-mass ratio achieve higher polar angles, hence, the envelope containing all the current of the family with the highest charge-to-mass ratio will enclose the whole beam. Plotting the trajectory of the mentioned envelope is a very easy way to evaluate the focusing effect of the beam due to the electrodes. Figure 3.19 shows that the beam emitted by the electrospray operating at 3000 V is narrower than the beam emitted when the electrospray was operating at 1200 V. Emitter potentials below 1200 V have not been considered because the electric field at the tip of the emitter would probably not be strong enough to shape the liquid into a Taylor cone. Emitter potentials above 3000 V have not been considered either because two-electrode electrosprays are not usually operated at such high voltages. Asymmetries in the geometry of the source could lead to shifting the emission point from the axis to the rim of the emitter, increasing the interception of the beam at the extracting electrode.

Figure 3.20a shows the velocity angle, defined in Eq. 3.2, distribution of these envelopes. All curves have the same shape, which means that the effect of the electric field induced by the electrodes is the same in all axial positions regardless of the emitter potential. The final polar angle of the curve associated with the electrospray operating at 3000 V is 13.83^{o} whereas the curve associated with an emitter potential of 1200 V is 24.48^{o}, a significant difference. The polar angle distribution across the axis is useful to observe the focusing effect of the electrodes but does not give a clear representation of the effect that increasing the emitter voltage has on the divergence of the beam. Figure 3.20b shows the final polar angle of each curve as a function of the emitter potential.

Taking a closer look at the initial velocity angle, the angle at which the droplets exit the inner region and enter the outer region, it can be seen that the curve associated with the lowest emitter voltage starts slightly further from the emission point than the one associated

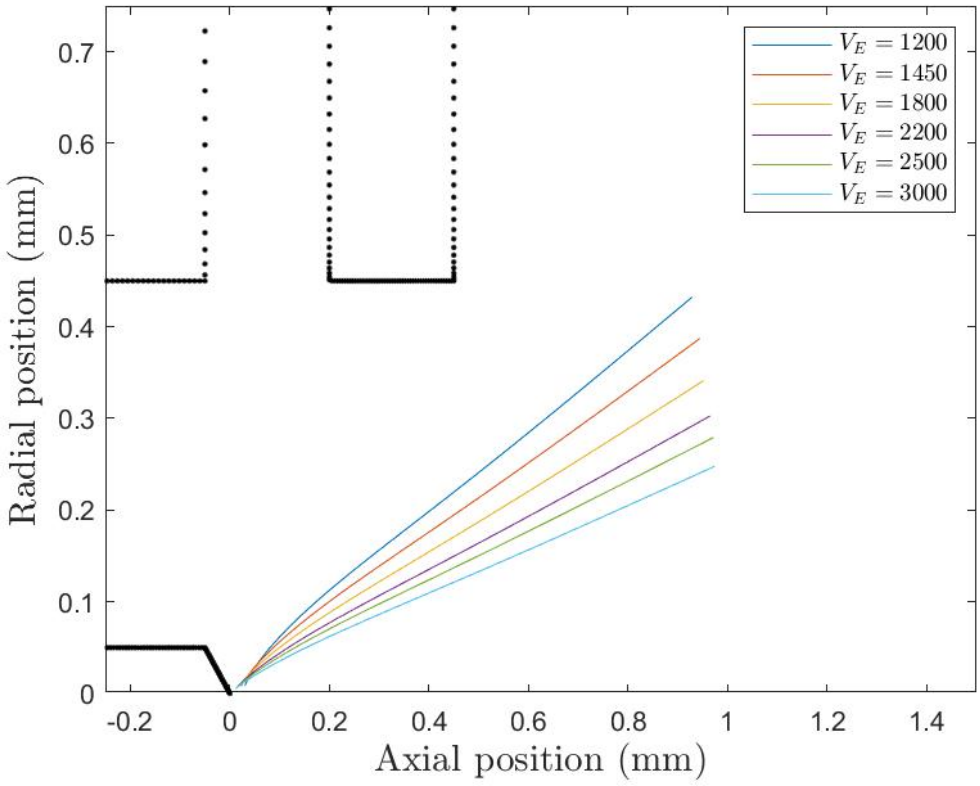

Figure 3.19: Envelope containing 98% of the current of the family with the highest charge-to-mass ratio ($\xi = 13037.66328\ C\,kg^{-1}$) for different emitter potential values V_E

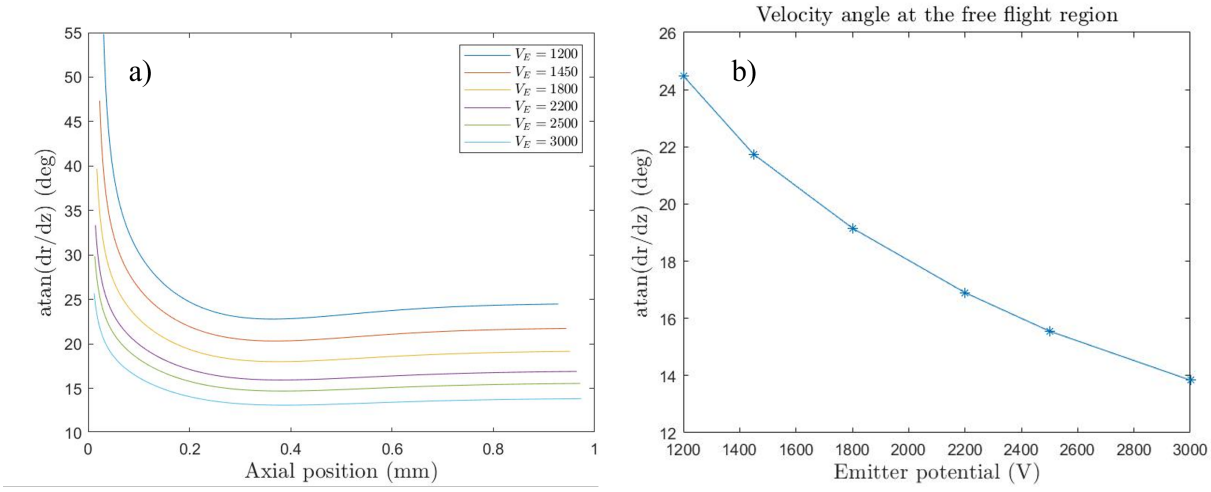

Figure 3.20: a) Velocity angle θ of the envelope containing 98% of the current of the family with the highest charge-to-mass ratio ($\xi = 13037.66328\ C\,kg^{-1}$) for different emitter potential values V_E b) Velocity angle at the free flight region for different emitter potential values V_E

with the highest emitter potential. This effect is caused by the jet's break-up position. The voltage drop associated with the losses occurring during the formation of the Taylor cone is the same for all cases, the one obtained experimentally with an electrospray operating at 1690V, but the potential across the axis changes according to the potential of the emitter. Nevertheless, this effect is negligible on the droplet distribution. One limitation of this study is that it assumes that the current of the beam is independent of the potential applied at the electrodes, which is not. It has been observed experimentally [7] that the current per emitter increases with the potential of the emitter at a fixed mass flow rate, which means that the average charge-to-mass ratio $< \xi >$ is increasing

$$< \frac{q}{m} >= \frac{I_b}{\rho Q} \tag{3.5}$$

If the average charge-to-mass ratio increases, we can expect the divergence of the beam to slightly increase too.

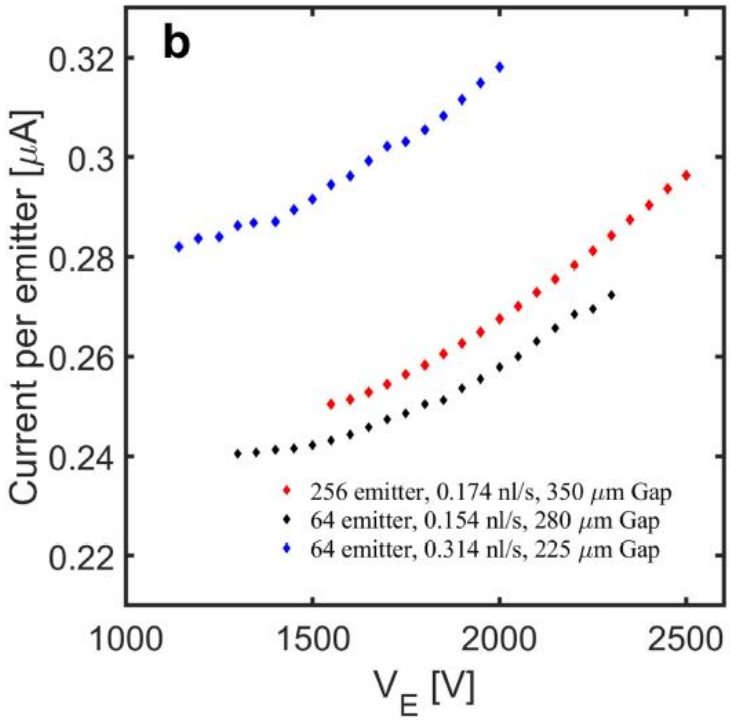

Figure 3.21: Variation of the current per emitter with emitter potential, for three different electrospray sources.

3.7 Geometry effects

It has been shown in Section 3.1 that the divergence of the beam mostly occurs because of the Coulombic repulsion between droplets at the very beginning of the emission. However, to show the effect that the extracting electrode has, different extractor configurations have been studied.

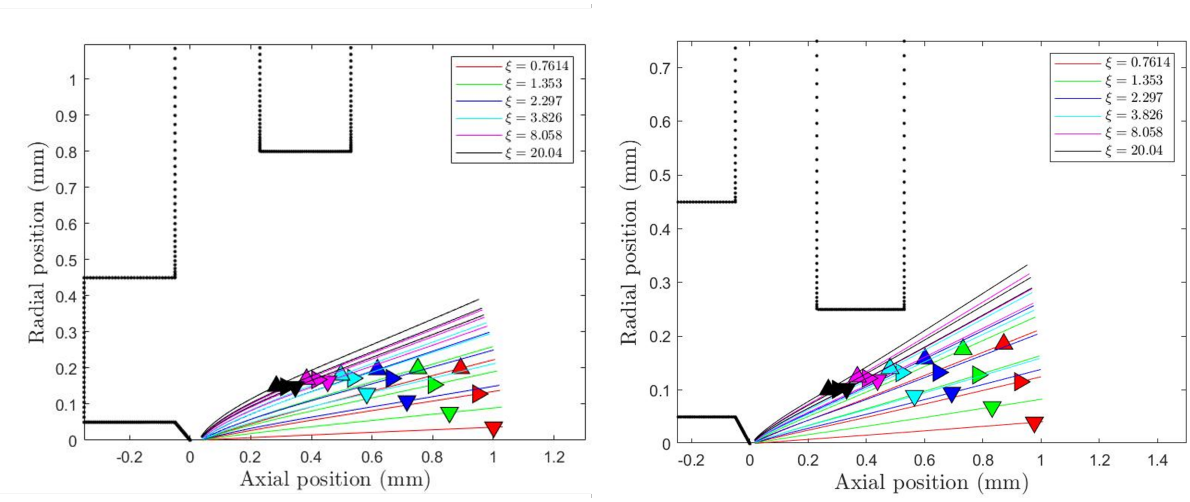

Figure 3.22: Simulation of two different extractor configurations

Figure 3.22 and Figure 3.23 show the comparison between a large extracting orifice, 800 μm diameter and a small one, 250 μm diameter. Both extracting electrodes are at the same distance from the emitter electrode, 280 μm. The geometry of the extractor changes the electric field induced at the tip of the emitter and as a consequence, the angle of the velocity close to the emission point. A larger orifice increases the radial electric field induced close to the emission point and causes droplets to achieve higher polar angles. However, Figure 3.23 shows an interesting result: the final velocity angle θ of all characteristics is only slightly affected. The final focusing effect is very similar in both configurations. Even if the focusing effect causes both configurations to achieve similar velocity angles at the free flight region, Figure 3.23 shows that it does not happen at the same rate. The configuration with a larger extracting orifice needs a longer axial distance to complete focusing the beam whereas the configuration with a smaller extracting orifice focuses it with half the length. Therefore,

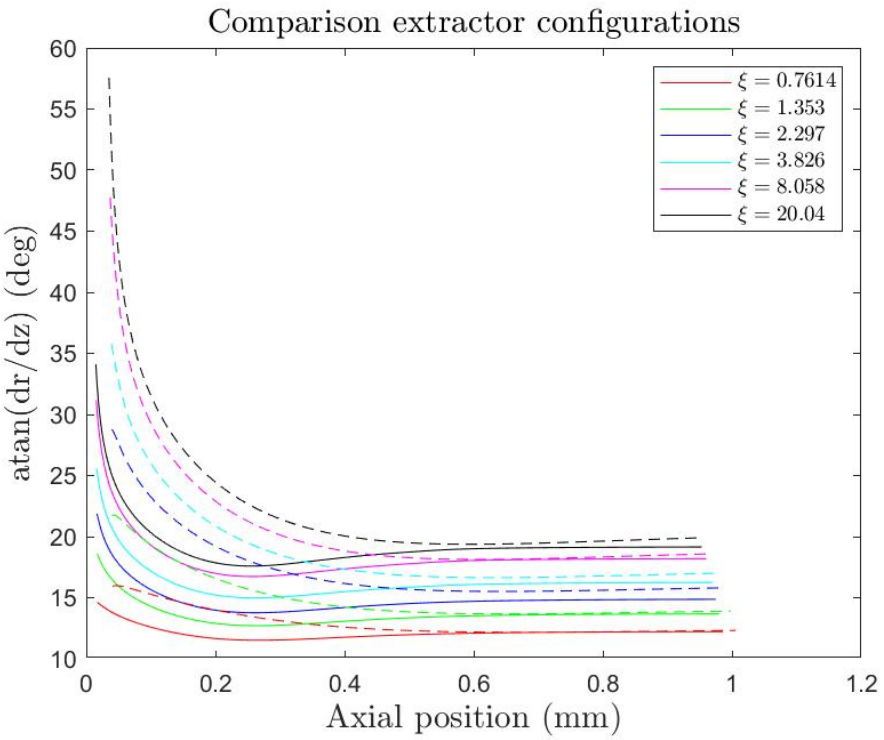

Figure 3.23: Velocity angle of the characteristics for two different extractor configurations. Dashed lines corresponds to a larger extractor orifice and solid lines to a smaller extractor orifice.

the beam emitted by the first configuration is broader because droplets expand radially at a higher rate during most of the emission.

Due to the difference in the position of the jet break-up, the curves associated with each configuration in Figure 3.23 do not originate from the same starting point.

3.8 Three electrode configuration

A third electrode is typically used to further accelerate emitted droplets and ions and increase the thrust T and the specific impulse I_{sp} of the electrospray thruster. An estimation of these values can be made with Eq (3.6) and Eq (3.7), where Eq (3.8) is used to estimate the average charge-to-mass ratio [30]. Notice that these computations do not account for many

effects that reduce the thrust efficiency. Even if these equations are estimations, they show that the thrust and specific impulse grow $\propto V_{acc}^{1/2}$

$$T \approx \dot{m} u_{ex} \approx \rho Q \sqrt{2 < \frac{q}{m} > V_{Acc}} \tag{3.6}$$

$$I_{sp} \approx \frac{T}{\dot{m} g_0} \approx \frac{1}{g_0} \sqrt{2 < \frac{q}{m} > V_E} \tag{3.7}$$

$$\frac{I}{\rho Q} =< \frac{q}{m} > \tag{3.8}$$

Figure 3.24 illustrates the behaviour, using the values for the electrospray simulated here ($I_{beam} = 300\, nA$, $Q = 0.266\, nl\, s^{-1}$ and $\rho = 1520\, kg\, m^{-3}$, the thrust would go from 0,62 μN operating with an accelerating voltage of 1600 V to 1.56 μN operating with a grounded accelerator and an emitter electrode at 10000V. The Isp, in the same way, would go from 157 s to 393 s.

Moreover, as we show in Figure 3.25, it also focuses the beam intensely, benefiting the performance of the system in two ways. Firstly, if the extractor orifices are well designed, the impingement will be minimal and the related problems already mentioned will be avoided. Secondly, most of the kinetic energy of the particles emitted will be axial kinetic energy, which is useful and produces thrust. Radial velocity does not produce thrust since it cancels due to axisymmetry, in other words, the loss of efficiency due to beam divergence is reduced.

It is worth mentioning that adding an accelerator is also beneficial for a thorough characterization of the electrospray source. Measuring the current intercepted on the extractor is crucial to evaluate the performance of the electrospray, the problem is that measuring such current is not easy due to facility effects. In a typical testing facility [7] the electrospray source is mounted inside a vacuum chamber facing a collector to intercept the beam. The

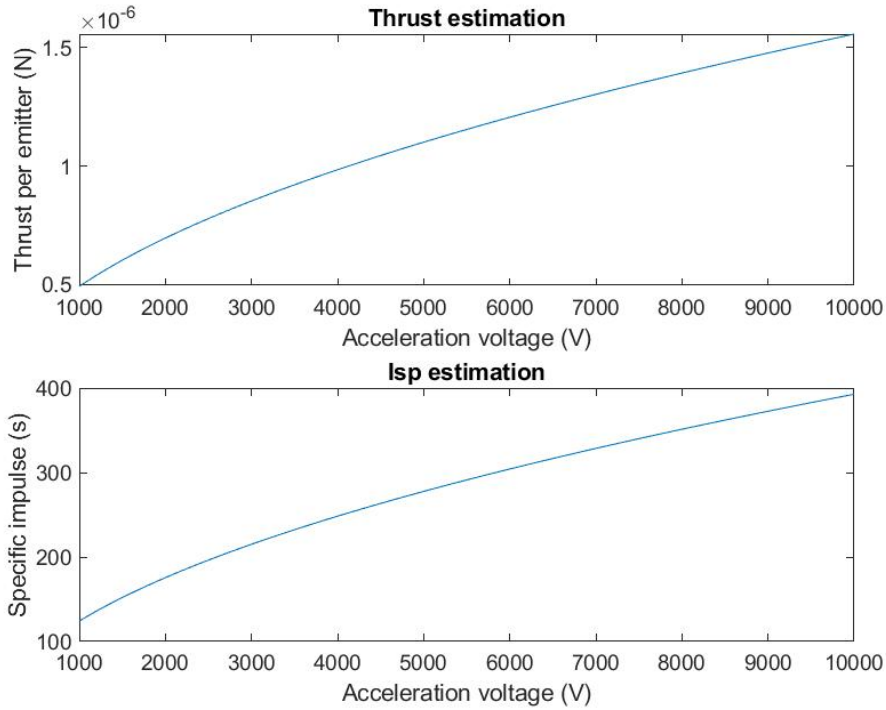

Figure 3.24: Estimation of Thrust and Isp through Eq. 3.6 and Eq. 3.7

propellant is fed to the electrospray source by pressurizing the reservoir, and electrometers are used to measure the currents at the electrodes and at the collector. A detailed explanation of the experimental setup will not be provided in this report as it falls beyond its scope. During the operation of the electrospray source, the beam is intercepted at the collector and high-energy particles give enough energy to electrons to break free. These electrons will come back to the source and will distort the measurements. To mitigate this problem a screen is added in front of the collector and is biased negatively to force them to come back to the beam target. However, it has also been reported that positive particles may be coming back to the source. That could be because the beam is colliding with the propellant accumulated at the beam target, causing splashes of positively charged particles that go back to the source [59], also distorting the measurements. Adding a third electrode shields the extractor from these secondary emissions and allows for a more accurate measurement of the real beam impingement.

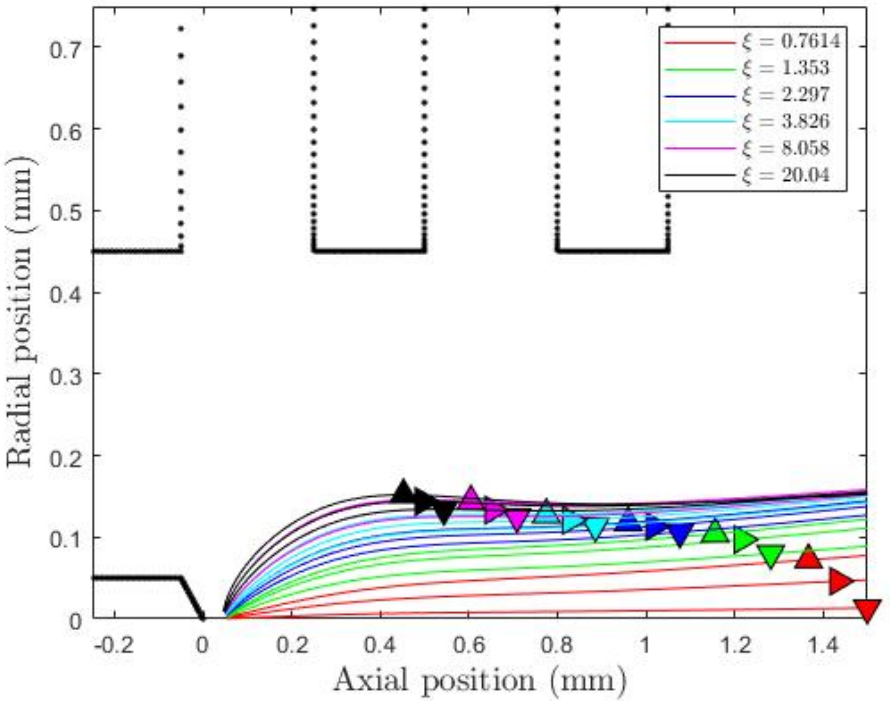

Figure 3.25: Envelopes containing 98%, 50% and 5% of the current of six representative groups with different charge-to-mass ratio (normalized with $\xi_J = 650.582\, C\, kg^{-1}$). Triangle pointing upwards, to the right and downwards, respectively.

We used the model to determine whether it was possible to add an acceleration electrode to our current geometry given the microfabrication constraints and to study how the beam would diverge in this three-electrode configuration. The emitter electrode is at an electric potential of 10000V and the extractor electrode is at 8400V, setting thus a potential difference between them of 1600V, a typical value of operation of electrospray thrusters in this configuration. The accelerator is grounded. Figure 3.25 shows that the current geometry is feasible, none of the characteristic curves intercepts the extracting electrodes. Even, if the actual beam was wider than in the simulation, there is a safety margin to avoid impingement problems. Figure 3.26 shows the strong focusing effect of the accelerator. All droplets reduce the local angle of the velocity θ to almost an axial trajectory. The focusing effect of the electrodes is strong enough to cause a "lens" effect, the droplets that are more sensitive to the electric field achieve negative radial velocities in some regions, which means

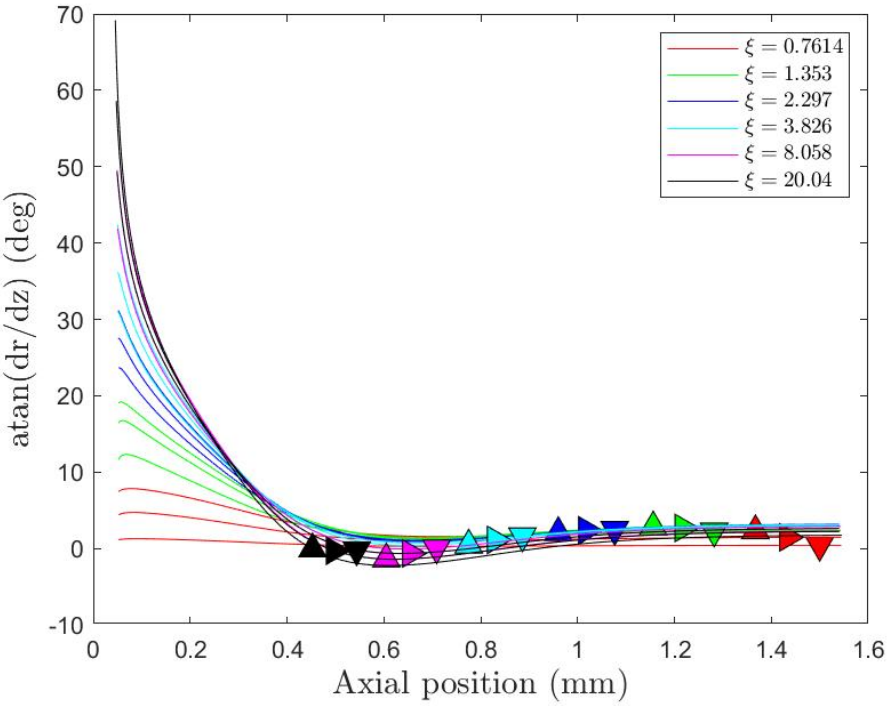

Figure 3.26: Velocity angle θ of the characteristics

that they stop diverging and they start getting closer to the axis. Such effect is also reflected in Figure 3.26, the angle of the velocity θ becomes negative for some groups of ξ in the region between the extractor and the accelerator. Figure 3.27 shows the radial component of the velocity of six representative groups with different charge-to-mass ratio (normalized with $\xi_J = 650.582\, C\, kg^{-1}$).

Figure 3.28 displays the total velocities for each group of charge-to-mass ratio. The segregation is similar to what was observed with the electrospray operating with a two-electrode configuration, Figure 3.10a, but the magnitude is much higher. The droplets of the representative group with the highest charge-to-mass ratio achieve 16 km/s and the biggest droplets 1.3 km/s.

The model needs experimental input data to compute a solution and this simulation has been done with the charge-to-mass ratio distribution obtained with an emitter operating at 1600V not 10000V, a better solution would be obtained with data obtained from a thruster

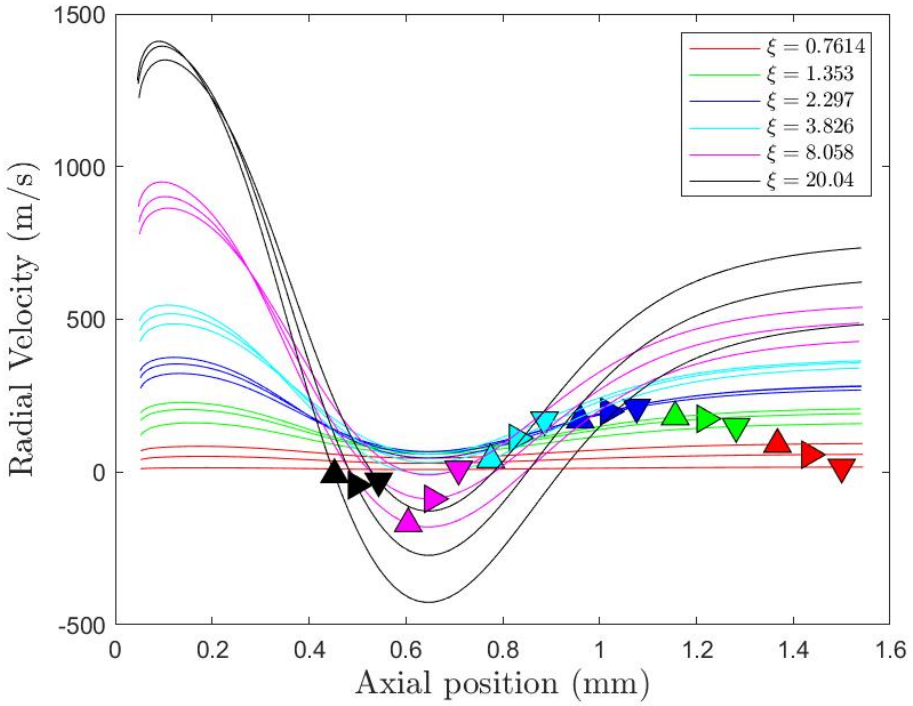

Figure 3.27: Radial velocity of six representative groups with different charge-to-mass ratio (normalized with $\xi_J = 650.582\, C\, kg^{-1}$). Triangle pointing upwards, to the right and downwards, respectively.

operating in this configuration. The jet oscillations are also calibrated with experimental data, therefore, also using the polar distribution of the beam measured for this latter configuration would lead to more accurate results. However, the focusing effect caused by the third electrode would be very similar.

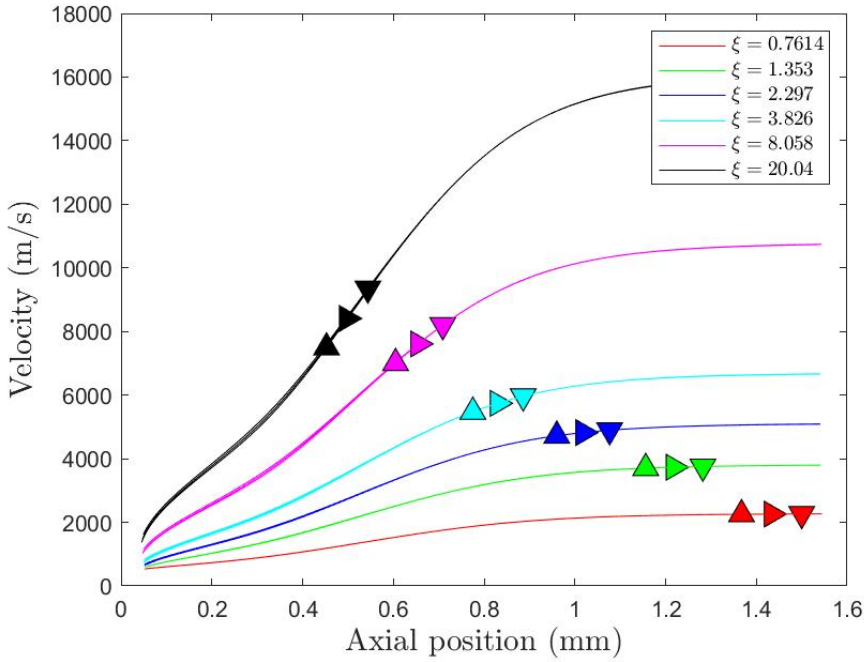

Figure 3.28: Velocity of six representative groups with different charge-to-mass ratio (normalized with $\xi_J = 650.582\, C\, kg^{-1}$). Triangle pointing upwards, to the right and downwards, respectively.

Chapter 4

Conclusions and Future Work

4.1 Conclusions

We present a model for electrospray beams that solves this problem as a continuum except near the emission region where, due to the high number density of droplets, retaining Coulomb pair-interactions between droplets is essential and a Lagrangian approach must be employed. At the boundary between the Lagrangian and Eulerian regions the former provides the initial conditions needed for solving the latter. Furthermore, because the space charge in both regions determines the electric field in either one, the algorithm for solving the problem uses an iterative scheme in which the different regions are solved sequentially, to provide estimates of the electric field of increasing accuracy. The analysis of the results at the inner region shows how the Coulomb interaction at the emission point gives rise to the droplet's angular segregation. Droplets with a higher charge-to-mass ratio have lower inertia and are more sensitive to the electric field, which causes them to suffer a higher deflection and achieve higher polar angles. On the other side, slower and bigger droplets are less affected by the radial electric field, their divergence is mostly caused by the oscillation of

the jet. This angular segregation is extended to the outer region because the focusing effect of two electrodes reduces the local angle of the velocity significantly but not completely. The model explains the paradoxical coincidence between the angular ranges of droplets and ions observed in experiments with the ionic liquid EMI-Im. The model shows that this is a consequence of the emission of ions from droplets in flight. If ions were emitted from the surface of the jet they would envelop the droplet beam, in contradiction with experiments.

The model requires the joint distribution of charge-to-mass ratio and diameters of the droplets. It also requires the initial velocity and position of the droplets upon emission from the jet. Time-of-flight and retarding potential diagnostics provide this key information. In addition, the droplets are naturally emitted with small radial offsets in their positions and velocities because of the oscillation of the jet. We do not have the ability to accurately predict these offsets, and instead, we model them with a random distribution based on two parameters, the maximum radius of the emission area and the maximum oscillation angle of the jet. The comparison between the experimental and calculated current density profiles guides the selection of these two parameters, which are found to have physical values.

The model has been applied to the geometry of the microfabricated electrospray source developed in our group to validate the design of the electrodes and minimize the interception of propellant by the extractor and accelerator. Over time, this creates conducting films that short the high voltage sources powering the electrodes, and the catastrophic failure of the electrospray thruster. However, the model does not predict any interception on the electrodes, but experiments do show a tiny fraction of intercepted current. The disagreement between experimental and simulated results could be caused by a misalignment between the emitters and the extractor orifices of the micromachined electrospray source, by other effects related to secondary emissions and ground testing problems or by an unknown phenomenon

that is not included in the beam model. In any case, further studies are required to reach a conclusion.

Different flow rates have been studied with the model and it has been observed that the beam divergence increases with the beam current due to the higher space charge density at the emission point. Experimentally the same behavior was observed. The model has also been used to illustrate and quantify the focusing effect caused by the electrodes. It has been shown that the beam gets significantly narrower when increasing the potential of the emitter. Furthermore, the effect of the geometry of the electrodes has been shown to modify the focusing effect of the electrodes but slightly affect the final local angle of the velocity.

Three important problems can also benefit from the beam model and further extend this research: a) investigating the interaction of the plumes of electrospray thrusters with the low density plasma that surrounds a spacecraft, and with its surfaces; b) the model can be extended to include viscous drag on the droplets, in order to study the deposition and coating of electrosprayed particles under atmospheric conditions and reduced pressures; c) in addition to beams similar to those of EMI-Im, the model can be used to study other emission modes such as the pure ion emission regime, mixed ion-droplet regimes with ions emitted from both droplets in flight and the base of the cone, electrosprays of droplets from liquids with lower electrical conductivities, etc. Each emission mode has characteristic initial conditions and distributions for the charged particles produced by the electrospray (these are also inputs to the model), which in turn depend on the physical properties and the flow rate of the liquid being electrosprayed.

4.2 Future Work

The scope of this thesis will be expanded to address the discrepancies observed between the model and experimental results, while also exploring additional operation configurations of interest. These configurations may involve different ionic liquids or electrode geometries. While the existing model did not predict any interception of the beam, experimental measurements have indicated the presence of beam interception. The objective is to enhance the model to achieve better alignment with the experimental findings.

Initially, the divergence between the model and experimental results may be attributed to potential droplet collisions at the emission point. It is possible that faster and smaller droplets are colliding with larger and slower droplets. These collisions could result in higher radial velocities and faster expansion of droplets in space. To investigate this phenomenon, a model will be developed to simulate these collisions and assess whether they contribute to the measured intercepted current.

Moreover, another potential reason for the mismatch between the model and experimental results could be erroneous experimental characterization. It is conceivable that the measured current at the extracting electrode is not solely derived from the beam but also influenced by facility effects. To address this, a comprehensive experimental characterization will be conducted, giving meticulous attention to facility effects. Various techniques will be employed to mitigate the impact of secondary emissions. These techniques include measuring the mass flux of particles returning from the beam target to the source and applying negative biasing to the beam target and screen to prevent electron backflow. Additionally, the micromachined electrospray source will be characterized using a three-electrode configuration, with the accelerator electrode shielding the first extracting electrode from secondary emissions. This setup will enable a more precise measurement of beam impingement.

Finally, the parameters used to model jet oscillations will be calibrated using experimental

measurements obtained from the MEMS electrospray source.

Bibliography

[1] Allied Market Research. Small satellite market: Global opportunity analysis and industry forecast, 2021-2030. `https://www.alliedmarketresearch.com/small-satellite-market`, August 2021.

[2] A. Bakr. *The Boundary Integral Equatio Method in Axisymmetric Stress Analysis Problems*, volume 14 of *Lecture Notes in Engineering*. Springer-Verlag Berlin Heidelberg, 1986. doi: 10.1007/978-3-642-82644-3.

[3] C. Barrios-Collado, G. Vidal-de Miguel, and P. M.-L. Sinues. Numerical modeling and experimental validation of a universal secondary electrospray ionization source for mass spectrometric gas analysis in real-time. *Sensors and Actuators B: Chemical*, 223:217–225, 2016.

[4] C. Brebbia and J. Dominguez. *Boundary Elements: An Introductory Course*. WIT Press, 1994. ISBN 9781853123498. doi: 10.1115/1.2897280.

[5] F. Chen, L. Lin, J. Zhang, Z. He, K. Uchiyama, and J.-M. Lin. Single-cell analysis using drop-on-demand inkjet printing and probe electrospray ionization mass spectrometry. *Analytical chemistry*, 88(8):4354–4360, 2016.

[6] A. Cisquella-Serra, M. Magnani, Á. Gual-Mosegui, S. Holmberg, M. Madou, and M. Gamero-Castaño. Study of the electrostatic jet initiation in near-field electrospinning. *Journal of colloid and interface science*, 543:106–113, 2019.

[7] A. Cisquella-Serra, M. Galobardes-Esteban, and M. Gamero-Castaño. Scalable microfabrication of multi-emitter arrays in silicon for a compact microfluidic electrospray propulsion system. *ACS Applied Materials & Interfaces*, 14(38):43527–43537, 2022.

[8] M. Cloupeau and B. Prunet-Foch. Electrohydrodynamic spraying functioning modes: a critical review. *Journal of Aerosol Science*, 25(6):1021–1036, 1994. doi: 10.1016/0021-8502(94)90199-6.

[9] J. F. De La Mora. The effect of charge emission from electrified liquid cones. *Journal of Fluid Mechanics*, 243:561–574, 1992.

[10] W. Deng and A. Gomez. Influence of space charge on the scale-up of multiplexed electrosprays. *Journal of Aerosol Science*, 38(10):1062–1078, 2007. doi: 10.1016/j.jaerosci.2007.08.005.

[11] J. Doshi and D. H. Reneker. Electrospinning process and applications of electrospun fibers. *Journal of electrostatics*, 35(2-3):151–160, 1995.

[12] J. B. Fenn. Electrospray wings for molecular elephants (nobel lecture). *Angewandte Chemie International Edition*, 42(33):3871–3894, 2003.

[13] J. B. Fenn, M. Mann, C. K. Meng, S. F. Wong, and C. M. Whitehouse. Electrospray ionization for mass spectrometry of large biomolecules. *Science*, 246(4926):64–71, 1989.

[14] J. Fernández de la Mora. The Fluid Dynamics of Taylor Cones. *Annual Review of Fluid Mechanics*, 39(1):217–243, 2007. ISSN 0066-4189. doi: 10.1146/annurev.fluid.39.050905.110159.

[15] W. M. Folkner, S. Buchman, R. L. Byer, D. B. DeBra, C. Dennehy, M. Gamero-Castano, J. Hanson, V. Hruby, G. M. Keiser, A. Kuhnert, et al. Disturbance reduction system: testing technology for precision formation control. In *High-Contrast Imaging for Exo-Planet Detection*, volume 4860, pages 221–228. International Society for Optics and Photonics, 2003. doi: 10.1117/12.457878.

[16] Fortune Business Insight. Small satellite market size, 2022-2029. `https://www.fortunebusinessinsights.com/industry-reports/small-satellite-market-101917`, September 2022.

[17] Frost Sullivan. Global satellite subsystem growth opportunities. `https://store.frost.com/global-satellite-subsystem-growth-opportunities.html`, March 2022.

[18] M. Gamero-Castaño. The structure of electrospray beams in vacuum. *Journal of Fluid Mechanics*, 604:339–368, 2008. doi: 10.1017/S0022112010003423.

[19] M. Gamero-Castaño. Characterization of the electrosprays of 1-ethyl-3-methylimidazolium bis(trifluoromethylsulfonyl) imide in vacuum. *Physics of Fluids*, 20 (3):032103, MAR 2008. ISSN 1070-6631. doi: 10.1063/1.2899658.

[20] M. Gamero-Castaño. Energy dissipation in electrosprays and the geometric scaling of the transition region of cone-jets. *Journal of Fluid Mechanics*, 662:493–513, 2010. doi: 10.1017/S0022112010003423.

[21] M. Gamero-Castaño. The expansion of colloid thruster beams and its dependence on emission temperature. *49th AIAA/ASME/SAE/ASEE Joint Propulsion Conference, San Jose, CA*, 2013. doi: 10.2514/6.2013-3880.

[22] M. Gamero-Castaño and A. Cisquella-Serra. Electrosprays of highly conducting liquids: A study of droplet and ion emission based on retarding potential and time-of-flight spectrometry. *Physical Review Fluids*, 6(1):013701, 2021.

[23] M. Gamero-Castaño and M. Galobardes-Esteban. Electrospray propulsion: Modeling of the beams of droplets and ions of highly conducting propellants. *Journal of Applied Physics*, 131(1):013307, 2022.

[24] M. Gamero-Castaño and V. Hruby. Electrospray as a source of nanoparticles for efficient colloid thrusters. *Journal of Propulsion and Power*, 17:977–987, 2001. doi: 10.2514/2.5858.

[25] M. Gamero-Castaño and M. Mahadevan. Sputtering yields of si, sic, and b 4 c under nanodroplet bombardment at normal incidence. *Journal of Applied Physics*, 106(5): 054305, 2009.

[26] M. Gamero-Castaño and J. Fernández de la Mora. Direct measurement of ion evaporation kinetics from electrified liquid surfaces. *Journal of Chemical Physics*, 113(2): 815–832, 2000.

[27] A. Gañán-Calvo, J. Lasheras, J. Dávila, and A. Barrero. The electrostatic spray emitted from an electrified conical meniscus. *Journal of aerosol science*, 25(6):1121–1142, 1994.

[28] A. Gañán-Calvo, J. López-Herrera, M. Herrada, A. Ramos, and J. Montanero. Review on the physics of electrospray: From electrokinetics to the operating conditions of single and coaxial Taylor cone-jets, and AC electrospray. *Journal of Aerosol Science*, 125:32–56, 2018. ISSN 00218502. doi: 10.1016/j.jaerosci.2018.05.002.

[29] A. M. Gañán-Calvo. Cone-Jet Analytical Extension of Taylor's Electrostatic Solution and the Asymptotic Universal Scaling Laws in Electrospraying. *Physical Review Letters*, 79(2):217–220, jul 1997. ISSN 0031-9007. doi: 10.1103/PhysRevLett.79.217.

[30] D. Goebel and I. Katz. *Fundamentals of Electric Propulsion: Ion and Hall Thrusters*. JPL Space Science and Technology Series. Wiley, 2008. ISBN 9780470436264.

[31] J. Grifoll and J. Rosell-Llompart. Efficient lagrangian simulation of electrospray droplets dynamics. *Journal of aerosol science*, 47:78–93, 2012. doi: 10.1016/j.jaerosci.2012.01.001.

[32] D. B. Hager, N. J. Dovichi, J. Klassen, and P. Kebarle. Droplet electrospray mass spectrometry. *Analytical Chemistry*, 66(22):3944–3949, 1994.

[33] R. Hartman, J.-P. Borra, D. Brunner, J. Marijnissen, and B. Scarlett. The evolution of electrohydrodynamic sprays produced in the cone-jet mode, a physical model. *Journal of electrostatics*, 47(3):143–170, 1999.

[34] R. P. Hartman, D. Brunner, D. Camelot, J. C. Marijnissen, and B. Scarlett. Jet break-up in electrohydrodynamic atomization in the cone-jet mode. *Journal of aerosol science*, 31(1):65–95, 2000.

[35] F. Higuera. Eulerian model of a dilute spray of charged droplets. *Journal of aerosol science*, 48:34–45, 2012. doi: 10.1016/j.jaerosci.2012.01.008.

[36] A. Jaworek. Electrospray droplet sources for thin film deposition. *Journal of materials science*, 42:266–297, 2007.

[37] J. Ju, Y. Yamagata, and T. Higuchi. Thin-film fabrication method for organic light-emitting diodes using electrospray deposition. *Advanced Materials*, 21(43):4343–4347, 2009.

[38] M. Jung, S. Kim, J. Lim, J. Lee, S. Jeong, D. Ku, S.-I. Na, and M. Kim. Droplet characterization of high-flowrate water electrospray using shadowgraph image analysis. *Journal of Mechanical Science and Technology*, 36(4):2139–2148, 2022.

[39] N. Kasoju and H. Ye. *Biomedical Applications of Electrospinning and Electrospraying*. Woodhead Publishing, 2021.

[40] R. Krpoun and H. R. Shea. Integrated out-of-plane nanoelectrospray thruster arrays for spacecraft propulsion. *Journal of Micromechanics and Microengineering*, 19(4):045019, mar 2009. doi: 10.1088/0960-1317/19/4/045019.

[41] R. S. Legge and P. C. Lozano. Electrospray propulsion based on emitters microfabricated in porous metals. *Journal of Propulsion and Power*, 27(2):485–495, 2011.

[42] G. Lenguito, J. F. de la Mora, and A. Gomez. Scaling up the power of an electrospray microthruster. *Journal of Micromechanics and Microengineering*, 24:055003, 2014.

[43] P. Lozano and M. Martínez-Sánchez. Ionic liquid ion sources: characterization of externally wetted emitters. *Journal of Colloid and Interface Science*, 282(2):415–421, 2005. ISSN 0021-9797. doi: https://doi.org/10.1016/j.jcis.2004.08.132.

[44] A. McEwen, H. Ngo, K. LeCompte, and J. Goldman. Electrochemical properties of imidazolium salt electrolytes for electrochemical capacitor applications. *Journal of the Electrochemical Society*, 146(5):1687–1695, 1999.

[45] S. Miller, J. Ulibarri-Sanchez, B. Prince, and R. Bemish. Capillary ionic liquid electrospray: beam compositional analysis by orthogonal time-of-flight mass spectrometry. *Journal of Fluid Mechanics*, 928:A12, 2021. doi: 10.1017/jfm.2021.783.

[46] A. A. Naqwi. In situ measurement of submicron droplets in electrosprays using a planar phase doppler system. *Journal of aerosol science*, 25(6):1201–1211, 1994.

[47] D. Obata, A. Nakamura, S. Katsuki, and H. Akiyama. Pulsed voltage driven electrospray. In *2012 IEEE International Power Modulator and High Voltage Conference (IPMHVC)*, pages 660–663. IEEE, 2012.

[48] H. Oh, K. Kim, and S. Kim. Characterization of deposition patterns produced by twin-nozzle electrospray. *Journal of Aerosol Science*, 39(9):801–813, 2008. doi: 10.1016/j.jaerosci.2008.05.003.

[49] D. Olvera-Trejo and L. Velásquez-García. Additively manufactured mems multiplexed coaxial electrospray sources for high-throughput, uniform generation of core–shell microparticles. *Lab on a Chip*, 16(21):4121–4132, 2016.

[50] M. Pulfer and R. C. Murphy. Electrospray mass spectrometry of phospholipids. *Mass spectrometry reviews*, 22(5):332–364, 2003.

[51] Research and Markets. Small satellite market, global forecast to 2028. `https://www.researchandmarkets.com/reports/5137212/small-satellite-market-by-mass-small-satellite`, March 2023.

[52] I. B. Rietveld, K. Kobayashi, H. Yamada, and K. Matsushige. Electrospray deposition, model, and experiment: toward general control of film morphology. *The Journal of Physical Chemistry B*, 110(46):23351–23364, 2006.

[53] J. Rosell-Llompart and J. Fernández de la Mora. Generation of monodisperse droplets 0.3 to 4 μm in diameter from electrified cone-jets of highly conducting and viscous liquids. *Journal of Aerosol Science*, 25(6):1093–1119, 1994.

[54] J. Rosell-Llompart, J. Grifoll, and I. Loscertales. Electrosprays in the cone-jet mode: From Taylor cone formation to spray development. *Journal of Aerosol Science*, 125: 2–31, 2018. doi: 10.1016/j.jaerosci.2018.04.008.

[55] F. Saiz and M. Gamero-Castaño. Atomistic modeling of the sputtering of silicon by electrosprayed nanodroplets. *Journal of Applied Physics*, 116(5):054303, 2014.

[56] K. Tang and A. Gomez. Generation by electrospray of monodisperse water droplets for targeted drug delivery by inhalation. *Journal of aerosol science*, 25(6):1237–1249, 1994.

[57] A. Thuppul, P. L. Wright, A. L. Collins, J. K. Ziemer, and R. E. Wirz. Lifetime considerations for electrospray thrusters. *Aerospace*, 7(8):108, 2020.

[58] A. Thuppul, A. Collins, P. Wright, N. Uchizono, and R. Wirz. Mass flux and current density distributions of electrospray plumes. *Journal of Applied Physics*, 130:103301, 09 2021. doi: 10.1063/5.0056761.

[59] N. Uchizono, A. Collins, C. Marrese-Reading, S. Arestie, J. Ziemer, and R. Wirz. The role of secondary species emission in vacuum facility effects for electrospray thrusters. *Journal of Applied Physics*, 130(14):143301, 2021.

[60] L. Yang, L. Sun, H. Zhang, F. Bian, and Y. Zhao. Ice-inspired lubricated drug delivery particles from microfluidic electrospray for osteoarthritis treatment. *ACS nano*, 15(12): 20600–20606, 2021.

[61] W. Yang, B. Lojewski, Y. Wei, and W. Deng. Interactions and deposition patterns of multiplexed electrosprays. *Journal of Aerosol Science*, 46:20–33, 2012. doi: 10.1016/j.jaerosci.2011.11.004.

[62] J. Ziemer, C. Marrese-Reading, C. Dunn, A. Romero-Wolf, C. Cutler, S. Javidnia, T. Li, I. Li, G. Franklin, P. Barela, O. Hsu, P. Maghami, J. O'Donnell, J. Slutsky, J. I. Thorpe, N. Demmons, and V. Hruby. Colloid microthruster flight performance results from space technology 7 disturbance reduction system. In *Proceedings of the 35th International Electric Propulsion Conference, Atlanta, GA, USA*, pages 8–12, 2017.

[63] J. K. Ziemer, T. M. Randolph, M. Gamero-Castaño, V. Hruby, W. Connolly, N. Demmons, E. Ehrbar, R. Martin, T. Roy, D. Spence, and J. Zwahlen. Flight hardware development of colloid microthruster technology for the space technology 7 and lisa missions. In *30th International Electric Propulsion Conference, Florence, Italy*, pages 2007–288, 2007.